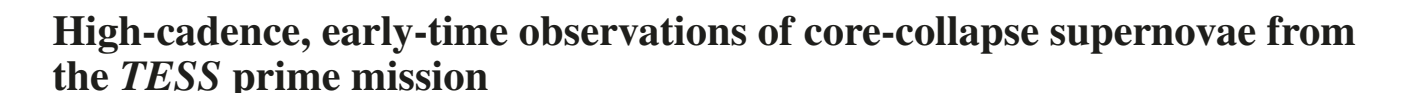
doi:10.1093/mnras/staa3675





P. J. Vallely , 1\* C. S. Kochanek, 1.2 K. Z. Stanek, 1.2 M. Fausnaugh, and B. J. Shappee<sup>5</sup>

Accepted 2020 November 17. Received 2020 November 13; in original form 2020 October 14

#### **ABSTRACT**

We present observations from the *Transiting Exoplanet Survey Satellite (TESS)* of twenty bright core-collapse supernovae with peak *TESS*-band magnitudes  $\lesssim$ 18 mag. We reduce this data with an implementation of the image subtraction pipeline used by the All-Sky Automated Survey for Supernovae (ASAS-SN) optimized for use with the *TESS* images. In empirical fits to the rising light curves, we do not find strong correlations between the fit parameters and the peak luminosity. Existing semi-analytic models fit the light curves of the Type II supernovae well, but do not yield reasonable estimates of the progenitor radius or explosion energy, likely because they are derived for use with ultraviolet observations while *TESS* observes in the near-infrared. If we instead fit the data with numerically simulated light curves, the rising light curves of the Type II supernovae are consistent with the explosions of red supergiants. While we do not identify shock breakout emission for any individual event, when we combine the fit residuals of the Type II supernovae in our sample, we do find a >5 $\sigma$  flux excess in the  $\sim$ 1 d before the start of the light-curve rise. It is likely that this excess is due to shock breakout emission, and that during its extended mission *TESS* will observe a Type II supernova bright enough for this signal to be detected directly.

**Key words:** techniques: photometric – methods: observational – stars: massive – supernovae: general – transients: supernovae.

### 1 INTRODUCTION

Core-collapse supernovae (SNe) are a broad class of astronomical transients produced by the explosion of high mass ( $\gtrsim 8\,\rm M_\odot$ ) stars at the end of their lives. The most common of these core-collapse subtypes, indeed the most common of all SNe subtypes in a volume-limited sample, are the Type II SNe (SNe II; Smartt et al. 2009; Li et al. 2011; Holoien et al. 2019a). The progenitors of these explosions are red supergiants with massive hydrogen envelopes that extend out to hundreds of solar radii (e.g. Smartt 2009, 2015), and they are empirically defined by the presence of hydrogen emission lines in their spectra (Filippenko 1997). Some SNe II show evidence of interaction with dense circumstellar material (CSM) in the form of narrow emission features, leading to their designation as SNe IIn (Schlegel 1990; Chugai & Danziger 1994).

While the majority of SNe in a volume-limited sample will be Type II SNe, about one-fifth of the sample will be comprised of Type Ib and Ic events (SNe Ib/c; Smartt et al. 2009; Li et al. 2011). These are defined by a lack of hydrogen in their spectra, and are further differentiated based on the presence (SNe Ib) or lack (SNe Ic) of strong helium lines. SNe Ib/c, often referred to as stripped-envelope SNe, are thought to be the core-collapse explosions of massive stars that have lost their hydrogen (and in the case of SNe Ic, helium)

\* E-mail: vallely.7@osu.edu

envelopes. One particularly interesting subclass of stripped-envelope SNe are the broad-lined SNe Ic (Ic-BL), which exhibit unusually broad absorption features and are sometimes associated with long-duration gamma-ray bursts (Galama et al. 1998; Stanek et al. 2003). Further complicating the landscape of core-collapse taxonomy are the Type IIb SNe, a subclass of stripped-envelope SNe that transition from resembling SNe II at early times to exhibiting the narrow helium emission of SNe Ib as they approach maximum light. The nearby SN 1993J is the well-studied archetype of these transitional events (Filippenko, Matheson & Ho 1993; Woosley et al. 1994; Maund et al. 2004; Stevance et al. 2020).

Building a theoretical understanding of the rising light curves of core-collapse explosions has been an area of intense research for some time, in large part because constraining progenitor properties through archival observations is difficult (see the reviews by Smartt 2009 and Smartt 2015). Nakar & Sari (2010) and Rabinak & Waxman (2011) explore semi-analytic approaches to this problem, assuming an idealized polytropic density profile for the stellar structure in order to make connections between the rising light curve and properties of the progenitor star. Whether or not these idealized profiles actually occur at relevant depths within the star remains an open question (Morozova et al. 2016), and numerical models provide a means of studying these explosions with fewer restrictive physical assumptions.

Detailed simulations have been used to model observations of particularly well-studied events like SN 1987A (Woosley 1988;

<sup>&</sup>lt;sup>1</sup>Department of Astronomy, The Ohio State University, 140 West 18th Avenue, Columbus, OH 43210, USA

<sup>&</sup>lt;sup>2</sup>Center for Cosmology and AstroParticle Physics, The Ohio State University, 191 W. Woodruff Ave., Columbus, OH 43210, USA

<sup>&</sup>lt;sup>3</sup>Department of Physics, Massachusetts Institute of Technology, Cambridge, MA 02139, USA

<sup>&</sup>lt;sup>4</sup>Kayli Institute for Astrophysics and Space Research, Massachusetts Institute of Technology, Cambridge, MA 02139, USA

<sup>&</sup>lt;sup>5</sup>Institute for Astronomy, University of Hawai'i, 2680 Woodlawn Drive, Honolulu, HI 96822, USA

Utrobin 1993; Utrobin et al. 2019), SN 1993J (Nomoto et al. 1993; Dessart et al. 2018), SN 1999em (Baklanov, Blinnikov & Pavlyuk 2005), and SN 2011dh (Bersten et al. 2012). Because these calculations are often tailored for the specific events, it is difficult to generalize their results. To this end, many studies have tried to develop a more general understanding of how characteristics of the progenitor star impact the resultant SN light curves. Examples include Young (2004), Kasen & Woosley (2009), Dessart et al. (2013), Sukhbold et al. (2016), and Curtis et al. (2020), and we make extensive use of the model light curves from Morozova et al. (2016) here. An excellent overview of our current understanding of core-collapse light-curve physics is provided in Chapters 5 and 9 of Branch & Wheeler (2017).

Early-time observations of SNe Ia have become increasingly accessible in recent years (e.g. Shappee et al. 2016; Stritzinger et al. 2018; Fausnaugh et al. 2019; Yao et al. 2019), but due to their lower intrinsic luminosities and faster rise times, the sample of core-collapse SNe observed at early times remains small. The first expected signature of these explosions occurs as the shock generated by the core-collapse approaches the surface of the progenitor, rapidly heating the photosphere to temperatures  $\gtrsim 10^5 \,\mathrm{K}$  and producing a short-lived outburst of high-energy radiation with a duration comparable to the star's light crossing time (e.g. Klein & Chevalier 1978; Ensman & Burrows 1992; Nakar & Sari 2010). This shock breakout emission has been seen by the GALEX satellite in the ultraviolet (UV) for a pair of SNe II (Schawinski et al. 2008; Gezari et al. 2015), and in x-rays by the Swift satellite for the Type Ib SN 2008D (Soderberg et al. 2008; Modjaz et al. 2009). In principle, this emission can also be seen in the optical and infrared (IR), but the weakness of the signature at these wavelengths coupled with its short duration ( $\lesssim$ 30 min at peak) makes it difficult to observe for even the highest cadence ground-based surveys.

Observations from the *Kepler* Space Telescope (Haas et al. 2010) and its extended *K2* mission were able to address both of these issues, as the mission provided high-quality photometry at an unprecedented 30-min cadence. In fact, the *Kepler* observations of the bright SN Ia ASASSN-18bt provide the highest precision light curve of any SN yet observed (Dimitriadis et al. 2019; Shappee et al. 2019). Two *Kepler* light curves of SNe II have been published by Garnavich et al. (2016), one of which shows a plausible detection of shock breakout emission.

In both the discovery of transiting exoplanets and the study of extragalactic transients, TESS is the natural successor to Kepler. The high-cadence TESS observations of the bright tidal disruption event ASASSN-19bt help to make it one of the best-studied optical TDEs to date (Holoien et al. 2019b), and Vallely et al. (2019) and Fausnaugh et al. (2019) have used TESS to study the early-time light curves of SNe Ia. In this paper, we present observations of twenty bright core-collapse SNe discovered over the course of the two year TESS prime mission. Although TESS images are deep enough to be competitive with current ground-based discovery surveys, there is a considerable delay between when observations are taken and when they are downlinked from the spacecraft and subsequently made available to the public. This delay is long enough that the mission is not an effective means of discovering bright long-lived transients. As such, all of the events in our sample were discovered by other surveys. It is critical that ground-based surveys quickly detect new transients in the TESS fields in order to enable follow-up spectroscopic confirmation and classification as well as multiband photometric monitoring.

For this reason, the All-Sky Automated Survey for Supernovae (ASAS-SN; Shappee et al. 2014; Kochanek et al. 2017; Holoien et al.

2019b) has been monitoring the TESS observing fields with increased cadence since the mission began. This monitoring programme has proven to be very successful. ASAS-SN discovered the unusual Type Ia SN ASASSN-18tb, the first extragalactic transient to be studied with TESS data (Vallely et al. 2019), the spectacular tidal disruption event ASASSN-19bt in the TESS continuous viewing zone Holoien et al. (2019b), as well as a large fraction of the bright SNe Ia from TESS Sectors 1-6 studied by Fausnaugh et al. (2019). During the second year of the mission, the Zwicky Transient Facility (ZTF; Bellm et al. 2019; van Roestel et al. 2019) also adopted this practice, and as a result these two surveys are responsible for discovering the majority of the bright transients that we study here. Additional discoveries were made during the course of standard operations by the Asteroid Terrestrial-impact Last Alert System (ATLAS; Tonry et al. 2018, 2 SNe), the  $D < 40 \,\mathrm{Mpc}$  SN Survey (DLT40; Tartaglia et al. 2018, 2 SNe), the Mobile Astronomical System of TElescope Robots (MASTER; Lipunov et al. 2010, 2 SNe), and from Gaia alerts (Gaia Collaboration et al. 2016, 1 SN).

Table 1 summarizes the observational properties of the events in our sample, including their discovery dates, spectroscopic classifications, redshifts, and V-band Galactic extinctions ( $A_V$ ; Schlegel, Finkbeiner & Davis 1998; Schlafly & Finkbeiner 2011). The bulk of the sample (12 of the total 20 events) is comprised of normal Type II SNe, and most of our subsequent analysis focuses on these events. The rest of the sample is made up of three Type IIn SNe, and one each of Type IIb, Ib, Ic, Ic-BL, and Ibn SNe. For inclusion in this study, we required that events have peak apparent TESS-band magnitudes  $\lesssim$ 18 mag, and the majority of the light curves we present reach peak magnitudes brighter than 17 mag. The most impressive individual light curve in our sample is that of the Type IIn SN DLT19c (SN 2019esa), which suffers from minimal TESS observing gaps and attains a peak magnitude of  $T_{\rm mag} = 13.83 \pm 0.01$ .

In Section 2, we describe our *TESS* image subtraction pipeline. We discuss empirical fits to the observed core-collapse *TESS* light curves in Section 3. In Section 4, we discuss semi-analytic models for the early-time light curves of the Type II SNe and the resulting estimates of the progenitor radii and explosion energies. We then compare our *TESS* light curves to the numerically simulated light curves from Morozova et al. (2016) and investigate their use as calibrators for the semi-analytic models. Section 5 discusses shock breakout emission and its likely detection in the stacked light curves of the SNe II in our sample. Finally, we discuss our results in Section 6.

# 2 TESS IMAGE SUBTRACTION LIGHT-CURVE GENERATION

There are a number of challenges associated with the TESS design that complicate the extraction of light curves and considerable effort has been expended by the community to develop pipelines to address them. The TESS Science Processing Operations Center (SPOC) pipeline generates calibrated light curves and validation products that are used by the TESS Science Office clearinghouse to identify promising transit candidates for additional follow-up. This pipeline is focused primarily on identifying transiting exoplanet signatures in the 200 000 stars selected for monitoring at 2-min cadence (Jenkins et al. 2016; Stassun et al. 2018). The TESS Asteroseismic Science Consortium (TASC) has produced its own pipeline, optimized for studying stellar oscillations, which computes light curves for all of the known stellar sources observed by TESS (Lund et al. 2017; Handberg & Lund 2019). While these pipelines are designed to produce light curves for known sources, the open-source ELEANOR package offers a publicly available tool for producing

Table 1. The twenty core-collapse SNe in our sample.

Supernova	TNS ID	Discovery date	Spectral classification	Redshift	$A_V$ (mag)
ASASSN-18qk	2018emt	2018-08-01 (Nicholls et al. 2018)	II (Onori et al. 2018a)	0.02395	0.068
ASASSN-18qv	2018eph	2018-08-04 (Brimacombe et al. 2018)	II (Onori et al. 2018b)	0.03	0.066
ZTF18abzscns	2018gxi	2018-09-28 (Fremling 2018)	II (Fremling, Dugas & Sharma 2018)	0.057	0.055
MASTEROT	2018jmt	2018-12-08 (Chasovnikov et al. 2018) Ibn (Castro-Segura et al. 2018)		0.036	0.327
J065447.10-593010.8					
DLT18ar	2018lab	2018-12-29 (Sand et al. 2018)	II (Razza et al. 2018)	0.0092	0.238
ATLAS19dzi	2019bwb	2019-03-17 (Tonry et al. 2019a)	IIn (Brinnel et al. 2019)	0.02019	0.536
ASASSN-19jy	2019dke	2019-04-11 (Brimacombe et al. 2019)	II (Holmbo et al. 2019)	0.01064	0.227
ATLAS19giz	2019dhz	2019-04-04 (Tonry et al. 2019b)	II (Fremling, Dugas & Sharma 2019)	0.034	0.214
DLT19c	2019esa	2019-05-06 (Sand et al. 2019)	IIn (Hiramatsu et al. 2019b)	0.00589	0.496
MASTEROT	2019fcc	2019-05-12 (Lipunov et al. 2019)	II (Gromadzki, Dong & Buckley 2019)	0.0126	1.079
J135130.87-525534.4					
ASASSN-19or	2019hcn	2019-06-08 (Castro et al. 2019)	II (Frohmaier et al. 2019)	0.018	0.309
Gaia19dcu	2019lqo	2019-07-21 (Hodgkin et al. 2019)	II (Bose et al. 2019)	0.0103	0.046
ZTF19abqhobb	2019nvm	2019-08-19 (Nordin et al. 2019)	II (Hiramatsu et al. 2019a)	0.01815	0.082
ZTF19abvdgqo	2019pfb	2019-09-01 (Forster 2019)	Ib (Terreran 2019)	0.03683	0.223
ASASSN-19acc	2019vxm	2019-12-01 (Cacella et al. 2019)	IIn (Leadbeater 2019)	0.019	0.282
ZTF20aagnbes	2020aem	2020-01-18 (Nordin et al. 2020a)	II (Dahiwale & Fremling 2020)	0.02218	0.116
ZTF20aahbamv	2020amv	2020-01-23 (Nordin et al. 2020b)	II (Irani et al. 2020)	0.0452	0.100
ZTF20aatzhhl	2020fqv	2020-03-31 (Forster et al. 2020b)	IIb (Zhang et al. 2020)	0.00752	0.089
ASASSN-20dn	2020euy	2020-03-23 (Brimacombe et al. 2020)	Ic (Tomasella et al. 2020)	0.06231	0.063
ZTF20abbplei	2020lao	2020-05-25 (Forster et al. 2020a)	Ic-BL (Burke et al. 2020)	0.03116	0.138

light curves of any source observed by *TESS* (Feinstein et al. 2019).

Ultimately, none of these pipelines are ideally suited for studying extragalactic transients with *TESS*. Because they generally are optimized for high-precision observations of short-duration signals associated with bright ( $T \lesssim 15 \, \mathrm{mag}$ ) stellar sources, their corrective procedures often weaken or entirely remove features that evolve on longer time-scales. This is a strength when searching for the fleeting flux dip during a planetary transit, but is clearly a problem when trying to study SNe.

We have developed our own pipeline for the primary purpose of studying transients with TESS. Producing TESS light curves using the image subtraction technique provides a natural means of addressing some of the otherwise troublesome characteristics of TESS images. Most notably, the large 21 arcsec pixels and undersampled point spread function (PSF) can make source blending a serious challenge for data reductions based on conventional aperture or PSF photometry techniques. This is not a problem for image subtraction, as light curves produced through this technique are sensitive only to changes in flux relative to the reference image.

We have applied many of the lessons learned from operating the All-Sky Automated Survey for Supernovae (ASAS-SN; Shappee et al. 2014; Kochanek et al. 2017) to develop an image subtraction pipeline optimized for use on the *TESS* full-frame images (FFIs). As in ASAS-SN data processing, the backbone of our *TESS* light curve generator is the ISIS image subtraction package (Alard & Lupton 1998; Alard 2000). We work with 750-pixel wide "postage stamps" cut out of the full FFIs. These postage stamps are generally centred on the location of the target, but are off-centred by necessity when the target is less than 375 pixels from a detector edge.

The basic automated image subtraction procedure we use to process the *TESS* FFIs broadly follows the standard ISIS package usage as follows:

- (1) Produce 750-pixel postage stamps from each of the FFIs.
- (2) Interpolate all images to the same astrometric solution.

- (3) Select 100 high-quality images for building the reference image.
- (4) Scale and subtract this reference image from all postage stamps.
  - (5) Perform PSF photometry on the subtracted images.

Images used to build the reference image must pass two tests. First, the associated FFI must not have any mission-provided data quality flags. This ensures that we avoid images compromised by momentum dumps and other issues described in the *TESS* Science Data Product Description Document. Secondly, the image must have PSF widths and sky background levels at or below the median values measured from all of that sector's images. This second test is important for excluding images with moderately elevated background counts due to scattered light from the Earth and Moon, as these FFIs are not always flagged by the mission. While they are not used to construct the reference image, these images can still be used in the light curves.

In general, this basic approach is fairly reliable. We used it to produce the first published *TESS* SN light curve (Vallely et al. 2019), observe the first promising repeating partial tidal disruption event candidate ASASSN-14ko (Payne et al. 2020), and study a sample of Southern Hemipshere  $\delta$  Scuti stars (Jayasinghe et al. 2019). However, it occasionally yields inconsistent results or artificial trends. One problem is the undersampled PSF of the *TESS* images. This makes it useful in some cases to convolve the images with a Gaussian prior to performing the image subtraction. Since this Gaussian smearing is flux-conserving, the only intrinsic drawback of the technique is that it slightly lowers the signal-to-noise ratio of the resulting light curve.

Light curves produced through this Gaussian smearing method have been used to study the tidal disruption event ASASSN-19bt (Holoien et al. 2019b), characterize the short-term variability of ESO-H $\alpha$  99's EXor outburst (Hodapp et al. 2019), and detect an 8.66-h periodicity in the light curve of V1047 Cen (Aydi et al. 2019). One

<sup>&</sup>lt;sup>1</sup>https://archive.stsci.edu/missions/tess/doc/EXP-TESS-ARC-ICD-TM-00 14.pdf

needs to be careful when using this technique, however. For targets located near other strongly variable sources, for example, applying the additional smearing will exacerbate signal pollution from the neighbouring source. Similar issues also arise if the target is close to a bright source, as the subtraction artifacts associated with the bright source can significantly degrade the target light curve after the Gaussian smearing is applied. Given the large pixel scale of *TESS*, these issues are not uncommon, so care must be taken on a sector-by-sector basis to gauge the utility of this correction.

While the Gaussian smearing technique is useful for mitigating issues with the undersampled PSF, the most significant problem with TESS observations have proven to be background artifacts produced by scattered light from the Earth and Moon (See, e.g. Section 7.32 of the TESS Instrument Handbook<sup>2</sup>) and the "strap" artifacts. These strap artifacts are produced by reflective metal straps located at the base of the silicon depletion region of the TESS detectors, and are most strongly present during epochs of significant scattered light (see Section 6.6.1 of the TESS Instrument Handbook for more details). The basic ISIS image subtraction procedure incorporates a 2-dimensional (2-D) polynomial sky model to remove differential background variations, but this sometimes proves insufficient for the complex scattered light structures present in TESS images. To address this, we developed an additional background filtering procedure, which has proven very effective at addressing these two issues

Our procedure uses one-dimensional median filters, applied once along each axis of the CCD, so that it captures background structure in both the vertical and horizontal directions of the detector. This dual median filtering is a simple, but effective, image processing technique that is applied to each postage stamp following the initial ISIS image subtraction. Our technique is described by the following steps:

- (1) Obtain the vertical (i.e. parallel to the straps) background template by measuring the median value in 30 pixel windows slid along each column of the postage stamp.
- (2) Subtract this vertical background template from the postage stamp, producing an image that has been median filtered along its columns.
- (3) Obtain the horizontal background template by measuring the median value in 30 pixel windows slid along each row of the 1-D median filtered image produced in Step 2.
- (4) Subtract this horizontal background template from the 1-D median filtered image to produce an image that has been median filtered along both axes.
- (5) Perform PSF photometry on the median filtered image produced in Step 4.

We favour this double 1-D filter approach rather than a single application of a 2-D filter because it provides an excellent means of removing CCD strap artifacts from the images. The initial column filtering allows us to remove the strap artifacts rather than blending them into the surrounding pixels, as occurs when a 2-D filter is used. Because the straps lie precisely along detector columns, the 1D filter applied in the vertical direction is able to effectively remove them. An example of this image processing sequence is shown in Fig. 1. Although developed independently, we note that this technique is similar to that utilized by Pál et al. (2020) for studying asteroids and other Solar system objects with *TESS*.

We use 30 pixels as the default width for the 1-D median filter, although this value can be easily increased as needed to accommodate brighter targets. In TESS images, 90 per cent of the total flux of a point-source is located within a  $2\times2$  pixel area (Ricker et al. 2015). Since the width of the median filter is considerably larger than 2 pixels and we are interested in relatively faint sources, the filtering should not – and does not appear to – remove appreciable amounts of source flux from the image. Whenever possible, the validity of this assumption is confirmed for each target by comparing the light curve measured after median filtering with that of the base-level reduction (see Fig. 2). For cases where it is evident that source flux was removed during the median filtering, the procedure is repeated using a median filter of larger width.

For each target, our automated image subtraction pipeline produces four light curves. The first is a basic ISIS reduction with neither of the *TESS*-specifc corrective techniques applied. The second and third are produced by either applying the Gaussian smearing or median filtering corrections separately. The final light curve is produced by combining both techniques, Gaussian smearing the postage stamps prior to performing image subtraction and applying median filtering to the subtracted images before performing PSF photometry. All four light curves are subsequently inspected manually, and the most appropriate reduction is selected for further analysis. Due to the reduced signal-to-noise ratio inherent to the technique, the light curves that utilize Gaussian smearing are only considered further if they appear necessary. Our preferred ordering is: (1) basic ISIS reduction, (2) median filtering only, (3) Gaussian smearing only, (4) both Gaussian smearing and median filtering.

Fig. 2 illustrates how important these corrective techniques can be, using the light curves of ASASSN-18qk, ZTF19abqhobb, and ASASSN-19or. The importance of the median filtering is particularly evident in ZTF19abqhobb, as the two reductions that do not include this correction are completely dominated by background artifacts. It is not clear, however, that the additional Gaussian smearing utilized in the dual correction reduction mitigates any artifacts not already removed by the median filtering. Thus, for this target, we select the median filter only reduction for subsequent analysis.

The differential light curves we produce measure changes in flux relative to the reference image. For transients like the SNe we study here, one would prefer to build a reference image exclusively using observations obtained long before the transient's rise. This ensures that no flux from the transient is present in the reference image. However, the relatively short 27 d monitoring window set by the *TESS* observing strategy means that this is not always possible. We address this concern by measuring the median value of the pre-rise flux measurements for each light curve and subtracting this flux value from all epochs. Introducing this flux offset shifts the entire light curve, ensuring it has a baseline of zero flux prior to the rise of the transient.

For transients observed by *TESS* over multiple sectors, it is in principle possible to generate a single reference image and then rotate it for use with each new pointing. In practice, however, the large pixel scale of the *TESS* observations makes this particularly difficult and introduces a large source of uncertainty. As in our prior work (e.g. Vallely et al. 2019; Holoien et al. 2019b; Tucker et al. 2020), we instead choose to construct independent reference images for each sector. When doing so, the flux offset of the first sector is determined from the pre-rise zero-point described above. For subsequent sectors, the flux offset is chosen such that linear extrapolations from the last  $\sim$ 2 d of the earlier sector and the first  $\sim$ 2 d of the later sector match.

In addition to the scattered light and strap artifacts described earlier, TESS images can be compromised by a number of issues,

<sup>&</sup>lt;sup>2</sup>https://archive.stsci.edu/files/live/sites/mast/files/home/missions-and-data/active-missions/tess/\_documents/TESS\_Instrument\_Handbook\_v0.1.pdf

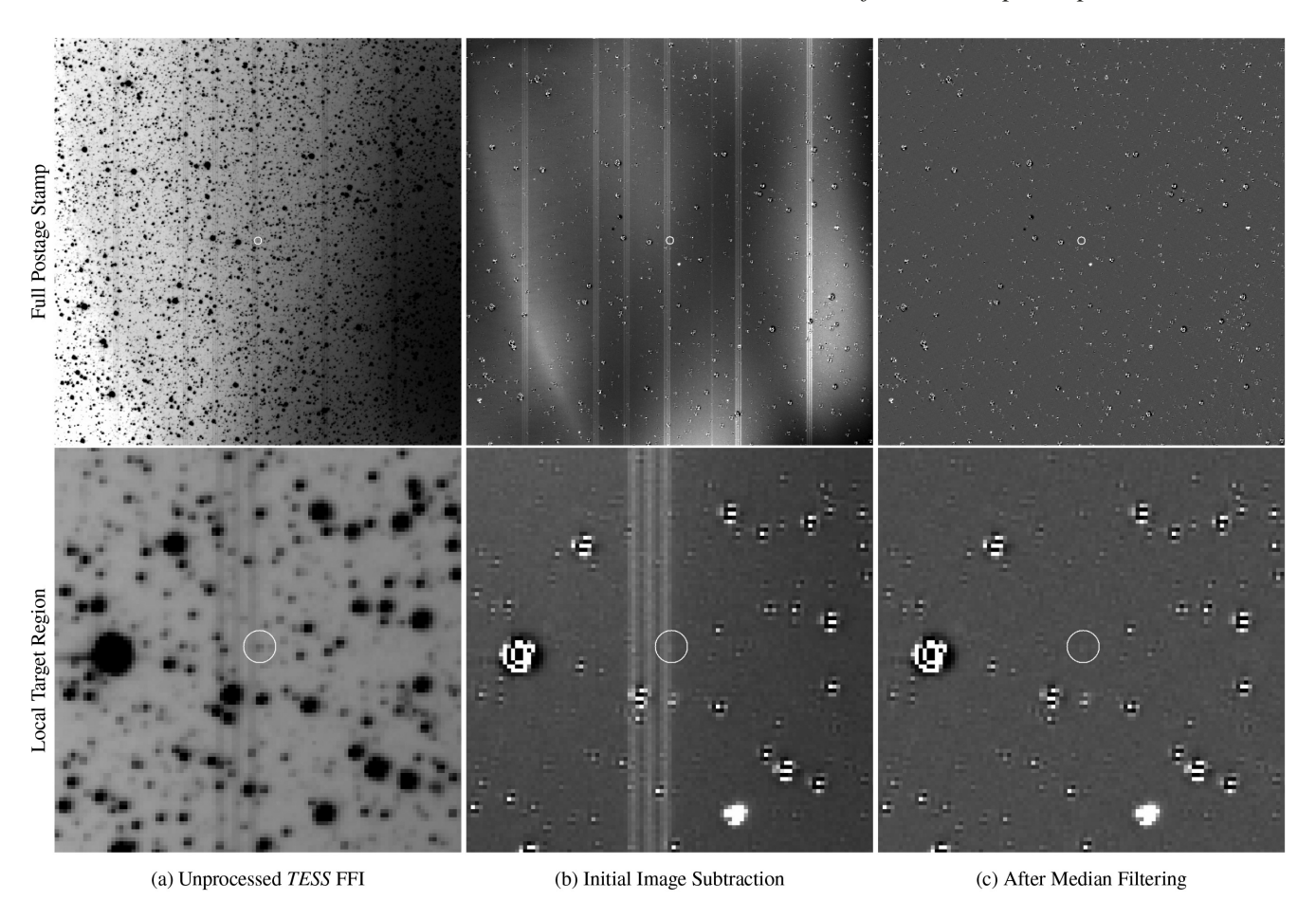
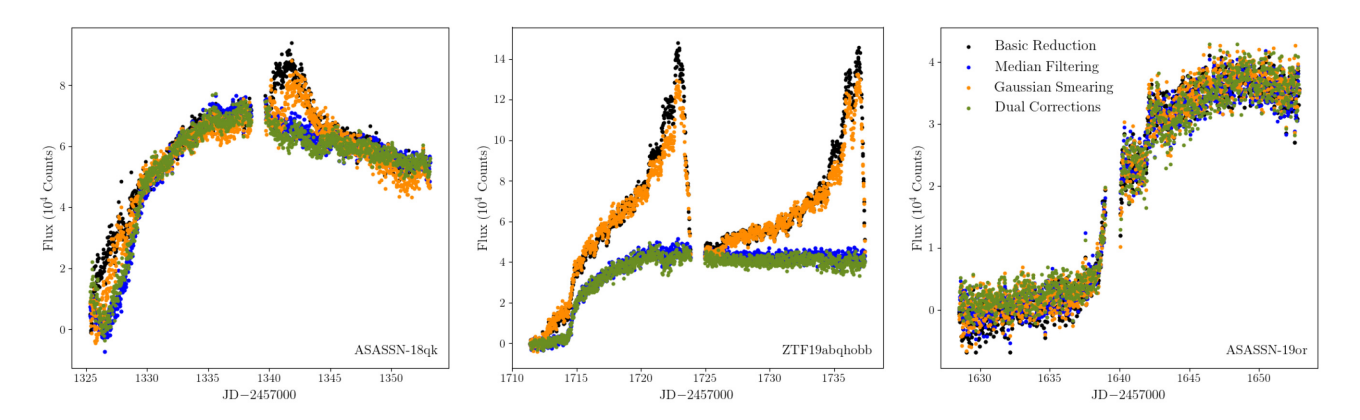


Figure 1. The image processing sequence for the *TESS* observation of ASASSN-18qk obtained on JD 2458341.51 by Camera 1/CCD 3. Column (a) shows the FFI as available for download from MAST, column (b) shows the subtracted image produced using the basic ISIS image subtraction, and column (c) shows the image produced after applying the median filtering technique described in Section 2. The images in columns (b) and (c) are shown using the same scale, which has a dynamic range about 25 times smaller than that used in column (a). The top row shows the full 750-pixel wide postage stamps, while the bottom row is now zoomed in on a  $100 \times 100$  pixel region centered on the location of ASASSN-18qk (circled in white). While the basic image subtraction process is able to effectively remove the large scale gradient visible in the FFI by fitting a low order polynomial to the differential background, it is clear that some of this background structure and the strap artifacts (the vertical lines) remain in the initial image subtraction. Both of these contaminants are removed after applying the median filtering technique.



**Figure 2.** The four light curves produced by our automated image subtraction pipeline for the *TESS* observations of the SNe ASASSN-18qk (left-hand panel), ZTF19abqhobb (middle), and ASASSN-19or (right-hand panel). In the cases of ASASSN-18qk and, particularly, ZTF19abqhobb, it is clear that incorporating median filtering in the processing sequence greatly improves the light-curve quality. In some cases, like ASASSN-19or, however, there is no clear benefit to the additional processing steps.

including the spacecraft's frequent momentum dumps, on board instrument anomalies, or ghost artifacts produced by nearby bright sources. Most of these issues are fairly well-understood and are discussed in the *TESS* Instrument Handbook and *TESS* Data Release Notes<sup>3</sup> documentation. While many of these conditions are noted by the mission provided quality flags that accompany the publicly available FFIs, it is often the case that non-flagged images are still compromised. For instance, the ASASSN-18qk FFI shown in Fig. 1 is not flagged by the mission.

The final step of our data reduction process is a manual vetting of the light curves to identify and remove any remaining compromised epochs. This is a somewhat subjective process, in which we examine light curves for epochs dominated by uncorrected systematics and remove them. In practice, these compromised epochs almost always coincide with either momentum dumps or issues with the observations documented in the Data Release Notes for the sector in question. We do not use photometry from these compromised epochs in our analysis, but for completeness they are included, but flagged, in the *TESS* light curves that we provide in the online supplementary material. The light curves for all of the core-collapse events in our sample are shown in Fig. 3.

#### 3 EMPIRICAL ANALYSIS OF LIGHT CURVES

In the literature, light-curve rises are commonly characterized using a single-component power law,  $f(t) \propto t^{\alpha}$  (See, e.g. Olling et al. 2015). While we prefer a slightly different treatment (described below), to facilitate comparisons with existing studies, we first fit the light curves as

$$f(t) = \frac{h}{(1+z)^2} \left(\frac{t-t_1}{1+z}\right)^{\alpha} + f_0, \tag{1}$$

for  $t > t_1$  and  $f(t) = f_0$  for  $t < t_1$ . Here,  $f_0$  is any residual background flux and  $t_1$  is the beginning of the model rise. The factors of 1 + z are introduced to account for redshift time-dilation, although this is a relatively small effect for this sample since all of the events are found at low redshift (z < 0.063). Following Olling et al. (2015) and Fausnaugh et al. (2019), we only fit the light curves up to 40 per cent of their peak flux. The resulting fit parameters are shown in Fig. 4, and best-fit  $\alpha$  values are presented in Table 2.

A single power law must eventually diverge from the actual light curve, forcing a somewhat arbitrary choice of a time to truncate the single power-law fits. We can minimize this problem by using curved power-law fits of the form

$$f(t) = \frac{h}{(1+z)^2} \left(\frac{t-t_1}{1+z}\right)^{a_1(1+a_2\cdot(t-t_1)/(1+z))} + f_0, \tag{2}$$

up to (near) the light-curve peak. The  $t_1$  and  $f_0$  parameters are the same, and at early times these fits become a  $f \propto t^{a_1}$  power law. The  $a_2$  term allows the model to follow the curvature of the light curve towards peak and so minimizes biases in estimates of the early time power-law exponent  $a_1$ . Mathematically,  $a_2$  is related to the rise time,  $t_{\rm rise} = t_{\rm peak} - t_1$ , between the start of the rise at time  $t_1$  and the time of the peak  $t_{\rm peak}$  by

$$a_2^{-1} = -t_{\text{rise}} \left[ 1 + \ln \left( t_{\text{rise}} \right) \right]. \tag{3}$$

Fitting  $a_2$  or some other variant of  $t_{\text{rise}}^{-1}$  has better error characteristics than trying to fit a parameter like  $a_2^{-1}$  because some fits allow  $a_2$  values consistent with zero when the TESS light curve does not

include the peak. For our estimates of  $t_{\rm rise}$ , we actually estimate  $t_{\rm peak}$  directly from the light curves as the time of peak flux in a rolling 6 h binned light curve rather than from the  $a_2$  values because we still only fit the curved power laws to near the time of peak and not over the peak – this would require a model with more parameters. Essentially, using the curved power-law parameter  $a_2$  to determine  $t_{\rm rise}$  suffers from the same sorts of biases as using the single power law does for estimates of  $\alpha$ . For most fits, however, the estimates of  $t_{\rm rise}$  from  $a_2$  are in rough agreement with our more direct estimates.

The curved power-law fits are shown by the red curves in Fig 3, and Fig 5 shows the peak absolute magnitude and rise time measured by *TESS* for each event as a function of the two curved power-law indexes,  $a_1$  and  $a_2$ . Different colours are used to differentiate between spectroscopic subtypes, although the only clear difference among them is that the CSM-interacting SNe IIn (shown in blue) exhibit substantially longer rise times. We exclude two events from this comparison: ASASSN-19acc because the *TESS* observations do not span the full rise to peak brightness, and Gaia19dcu because it was already rising at the start of its *TESS* observations. We still obtain fits for these two events, and for completeness their parameters are reported along with those of the rest of the sample in Table 2. For comparison, Fig. 5 also includes the results from fitting the same curved power law to the numerical model light curves from Morozova et al. (2016). These models are discussed in detail in Section 4.2.

The single-component power law's  $\alpha$  parameter and the curved power-law's  $a_1$  parameter should be closely related, and Fig. 6 compares their best-fitting values for the well-observed events in our sample. For light curves where  $\alpha$  is well-constrained, the best-fitting  $\alpha$  values agree very well with the best-fitting  $\alpha$  values. In cases where  $\alpha$  is not well-constrained, however, the best-fitting  $\alpha$  values are consistently and systematically larger than the best-fitting  $a_1$  values. This suggests that, in addition to the avoidance of an arbitrary end point, curved power-law fits may provide a more robust means of characterizing early-time light curves than the single-component power law (equation 1).

There does not appear to be a strong correlation between the empirical light-curve fit parameters and their peak luminosities or rise times, at least not in this sample. There is a tendency for larger values of  $a_1$  to correspond to brighter peak luminosities in the Morozova et al. (2016) light curves, but this trend is much weaker in the observed sample (Pearson's r = -0.56; p = 0.012). As described above, in the curved power-law formalism  $a_2$  is directly linked to the light-curve rise time, and we do see some of this expected correlation in Fig. 5 (Pearson's r = 0.59; p = 0.007), but the quantitative agreement is poor compared to the uncertainties, confirming the need for a more complex empirical model if the fits are to be used to estimate the rise time.

# 4 COMPARISON TO THEORETICAL MODELS

Next, we compare our *TESS* observations to several theoretical models. First, following Garnavich et al. (2016), we use the semi-analytic treatments of Nakar & Sari (2010) and Rabinak & Waxman (2011). Next, we examine the more detailed numerical simulations of Morozova et al. (2016). Finally, we investigate using the simulated light curves to calibrate the semi-analytic treatments.

## 4.1 Semi-analytic models

We first analyse our *TESS* data using the same semi-analytic models that Garnavich et al. (2016) used when studying KSN2011a and KSN2011d. The Rabinak & Waxman (2011) and Nakar & Sari (2010)

<sup>&</sup>lt;sup>3</sup>https://archive.stsci.edu/tess/tess\_drn.html

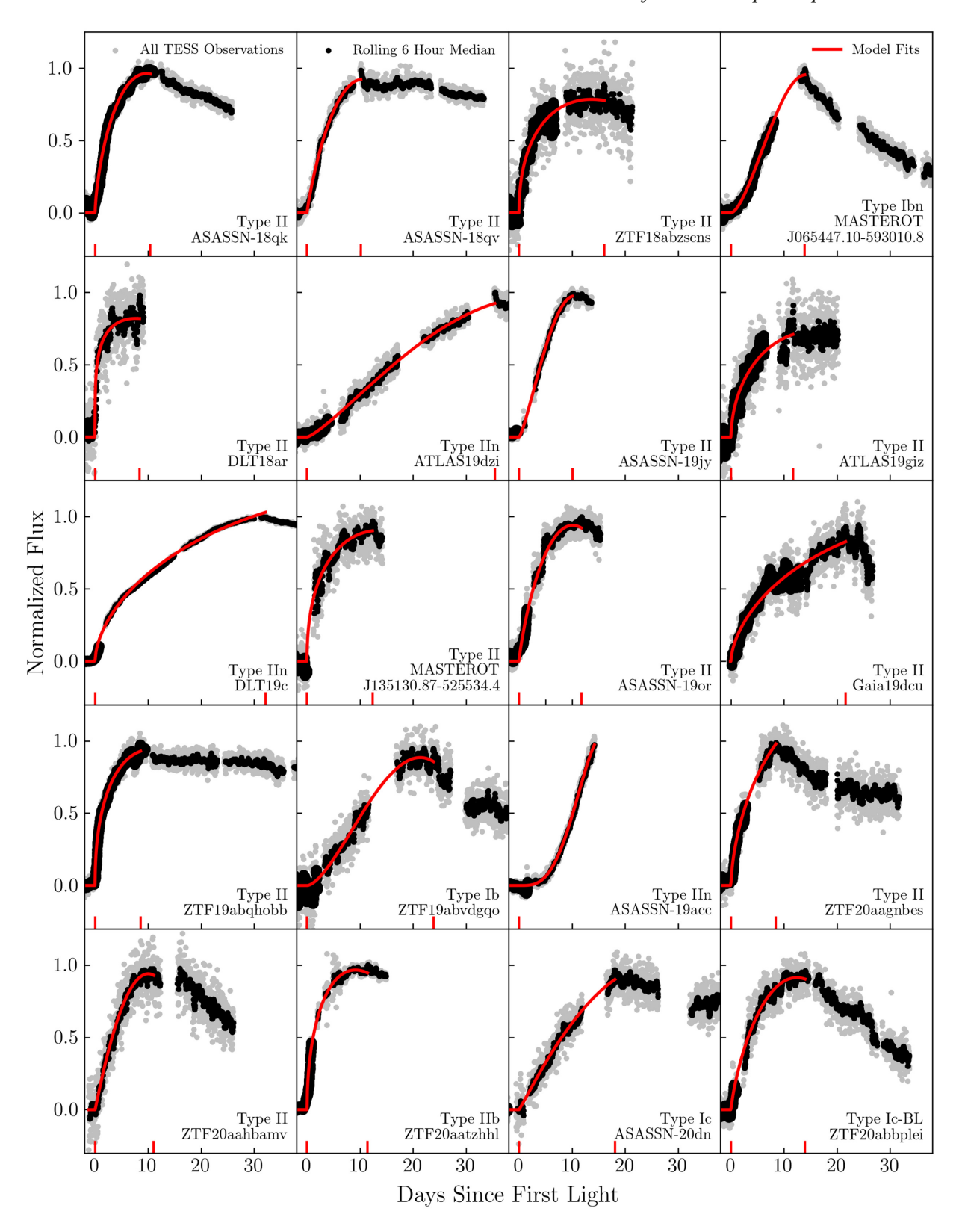


**Figure 3.** TESS light curves of the twenty core-collapse events in our sample. For each event, all of the TESS observations are shown in grey, with their rolling 6 h median shown in black, and the best-fit model (equation 2) for the rising light curve is shown in red. The two red tick marks at the bottom of each panel indicate the times of first and maximum light for each light curve. All of these light curves are included in machine-readable format in the online supplementary material.

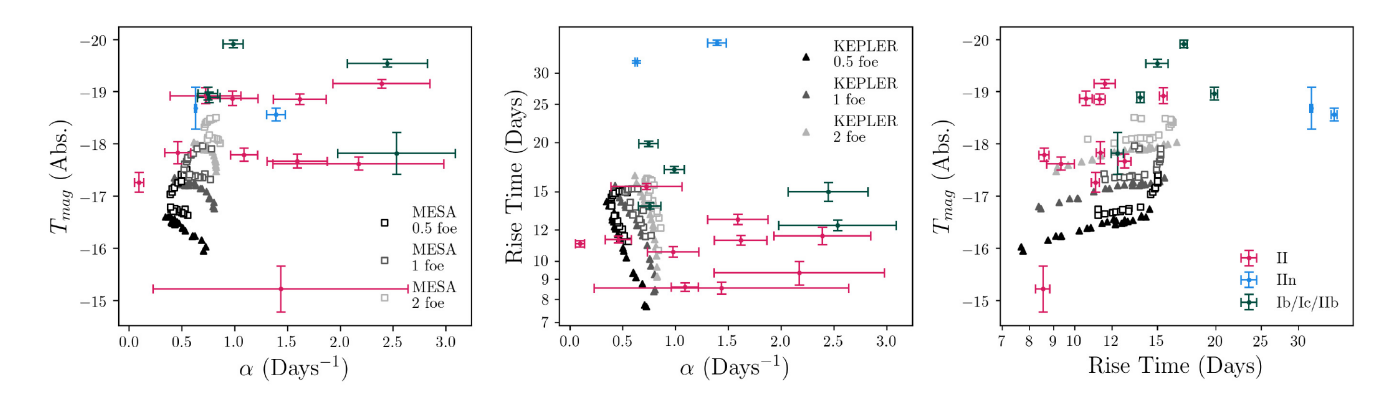


**Figure 4.** Single-component power-law fit parameters compared to rise time and *TESS*-band absolute magnitude for the core-collapse events in our sample as well as a suite of models computed by Morozova et al. (2016) from which we calculate synthetic *TESS* observations. The coloured points indicate observed data, with SNe II in dark red, SNe IIn in light blue, and SNe Ib/c and IIb in dark green. The shaded points indicate model light curves. Progenitors simulated using MESA are shown as open squares and those simulated using KEPLER are shown as solid triangles. Explosion energy is indicated by shading, with lighter shades corresponding to higher explosion energy.

Table 2. TESS light-curve parameters.

Supernova	Peak magnitude (Apparent)	Peak magnitude (Absolute)	Rise time (Days)	$t_1$ (TJD)	α	$a_1$	$a_2 \times 100$ (Days <sup>-1</sup> )
ASASSN-18qk	$16.19 \pm 0.04$	$-18.85 \pm 0.10$	$10.2 \pm 0.21$	$1327.40 \pm 0.02$	$1.62 \pm 0.25$	$0.68 \pm 0.02$	$-4.27 \pm 0.14$
ASASSN-18qv	$16.31 \pm 0.04$	$-19.22 \pm 0.08$	$9.9 \pm 0.21$	$1329.73 \pm 0.04$	$2.39 \pm 0.46$	$0.88 \pm 0.03$	$-4.61 \pm 0.20$
ZTF18abzscns	$18.05 \pm 0.15$	$-18.92 \pm 0.15$	$15.2 \pm 0.21$	$1387.45 \pm 0.05$	$0.73 \pm 0.33$	$0.45 \pm 0.03$	$-2.41 \pm 0.28$
MASTEROT	$16.86 \pm 0.06$	$-19.22 \pm 0.09$	$13.4 \pm 0.32$	$1455.51 \pm 0.24$	$2.45 \pm 0.38$	$1.68 \pm 0.11$	$-4.60 \pm 0.18$
J065447.10-593010.8							
DLT18ar	$17.55 \pm 0.16$	$-15.48 \pm 0.29$	$8.3 \pm 0.21$	$1480.90 \pm 0.01$	$1.44 \pm 1.21$	$0.23 \pm 0.03$	$-2.43 \pm 0.76$
ATLAS19dzi	$16.33 \pm 0.04$	$-18.56 \pm 0.12$	$34.7 \pm 0.34$	$1551.30 \pm 0.27$	$1.39 \pm 0.09$	$1.28 \pm 0.04$	$-1.32 \pm 0.08$
ASASSN-19jy	$15.80 \pm 0.02$	$-17.61 \pm 0.20$	$10.0 \pm 0.24$	$1581.98 \pm 0.12$	$2.55 \pm 0.77$	$1.34 \pm 0.05$	$-5.58 \pm 0.13$
ATLAS19giz	$18.06 \pm 0.20$	$-17.83 \pm 0.21$	$11.3 \pm 0.23$	$1575.48 \pm 0.09$	$0.46 \pm 0.12$	$0.53 \pm 0.08$	$-2.16 \pm 0.97$
MASTEROT	$16.99 \pm 0.09$	$-17.26 \pm 0.19$	$12.2 \pm 0.21$	$1609.65 \pm 0.01$	$0.10 \pm 0.04$	$0.44 \pm 0.03$	$-2.23 \pm 0.39$
J135130.87-525534.4							
DLT19c	$13.83 \pm 0.01$	$-18.40 \pm 0.37$	$32.0 \pm 0.21$	$1608.94 \pm 0.01$	$0.63 \pm 0.01$	$0.57 \pm 0.01$	$-0.53 \pm 0.02$
ASASSN-19or	$16.86 \pm 0.05$	$-17.67 \pm 0.13$	$11.5 \pm 0.22$	$1637.49 \pm 0.06$	$1.59 \pm 0.29$	$0.83 \pm 0.03$	$-4.57 \pm 0.16$
Gaia19dcu	<16.51	<-16.65	>21.4	$1683.45 \pm 0.10$	$0.64 \pm 0.08$	$0.59 \pm 0.07$	$-0.76 \pm 0.32$
ZTF19abqhobb	$16.64 \pm 0.03$	$-17.79 \pm 0.13$	$8.4 \pm 0.21$	$1714.34 \pm 0.01$	$1.09 \pm 0.13$	$0.44 \pm 0.01$	$-2.91 \pm 0.26$
ZTF19abvdgqo	$17.11 \pm 0.10$	$-18.96 \pm 0.12$	$23.0 \pm 0.55$	$1721.88 \pm 0.51$	$0.75 \pm 0.09$	$1.65 \pm 0.10$	$-3.02 \pm 0.07$
ASASSN-19acc	<15.63	<-19.01	>13.9	$1800.79 \pm 0.48$	$1.51 \pm 0.03$	$3.52 \pm 0.23$	$-5.05 \pm 0.07$
ZTF20aagnbes	$17.27 \pm 0.07$	$-17.62 \pm 0.12$	$8.3 \pm 0.21$	$1866.02 \pm 0.03$	$2.17 \pm 0.81$	$0.61 \pm 0.04$	$-1.78 \pm 0.84$
ZTF20aahbamv	$17.60 \pm 0.13$	$-18.87 \pm 0.14$	$10.6 \pm 0.26$	$1871.67 \pm 0.16$	$0.98 \pm 0.24$	$1.02 \pm 0.07$	$-5.25 \pm 0.30$
ZTF20aatzhhl	$14.77 \pm 0.02$	$-17.74 \pm 0.29$	$11.3 \pm 0.21$	$1939.98 \pm 0.01$	$2.53 \pm 0.56$	$0.49 \pm 0.01$	$-3.62 \pm 0.11$
ASASSN-20dn	$17.26 \pm 0.06$	$-19.91 \pm 0.07$	$17.0 \pm 0.30$	$1914.61 \pm 0.21$	$0.99 \pm 0.10$	$1.05 \pm 0.07$	$-2.05 \pm 0.28$
ZTF20abbplei	$16.77 \pm 0.07$	$-18.89 \pm 0.10$	$13.5\pm0.22$	$1994.63\pm0.06$	$0.76\pm0.11$	$0.79\pm0.03$	$-3.66 \pm 0.16$

*Note.* Absolute magnitudes reported here account for Galactic extinction and include a  $300 \,\mathrm{km} \,\mathrm{s}^{-1}$  uncertainty due to peculiar velocities, except for the three events at z < 0.01 for which we have used the Theureau et al. (2007) Tully–Fisher relation distance estimates. TJD is a standard time for *TESS* data, defined as JD  $- 2457\,000.0\,\mathrm{d}$ . We exclude Gaia19dcu and ASASSN-19acc from our analysis because their rising *TESS* light curves are incomplete.

models describe core-collapse explosions as a time-dependent black-body parametrized by the explosion energy, the density structure and opacity of the ejecta, and the mass and radius of the stellar progenitor. If one makes some reasonable assumptions about the ejecta and assumes a fixed progenitor mass, the models depend primarily on the explosion energy and progenitor radius. The model radius largely determines the light-curve rise time, and the explosion energy largely determines the peak luminosity. In principle, these models should be a good tool for estimating these generally inaccessible parameters of the explosion when coupled with high cadence *TESS* or *Kepler* light curves.

For our analysis, we use semi-analytic models that assume a power-law density structure with an index of n = 3/2, appropriate for the efficiently convective envelopes of red supergiant stars (RSGs).

For the Nakar & Sari (2010) model these are simply their equations (29) and (31). Some care must be taken when using the temperature description from Rabinak & Waxman (2011), however, as the unmodified  $T_{\rm ph}$  from equation (13) does not describe the observed blackbody. This is instead described by the colour temperature,  $T_{\rm col}$ , and for the relevant timescales,  $T_{\rm col}\approx 1.23T_{\rm ph}$  (see Rabinak & Waxman's fig. 1). Thus, for the Rabinak & Waxman (2011) model, we use their equations (13) and (14) and include the 1.23 scaling factor to convert  $T_{\rm ph}$  to  $T_{\rm col}$ . We then assume a fully ionized hydrogen envelope (with opacity  $\kappa=0.34\,{\rm cm^2\,g^{-1}}$ ) and set the normalization of the ejecta density to  $f_p=0.1$ , a value consistent with RSG progenitors (Calzavara & Matzner 2004). We also assume a progenitor mass of  $12.5\,{\rm M}_{\odot}$ , although we note that there is little difference if we instead use  $15\,{\rm M}_{\odot}$  like Garnavich et al. (2016).

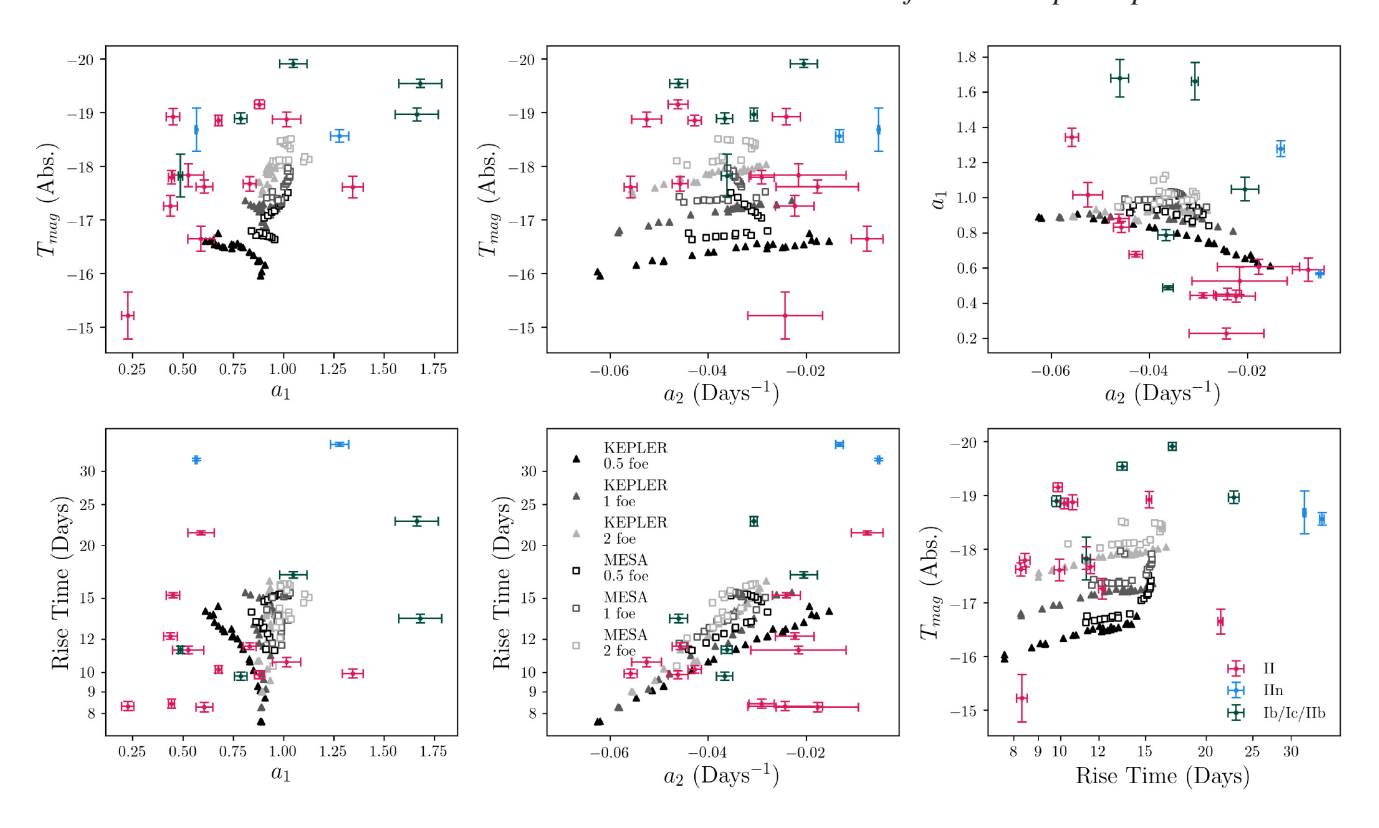


**Figure 5.** Curved power-law fit parameters compared to rise time and *TESS*-band absolute magnitude for the core-collapse events in our sample as well as a suite of models computed by Morozova et al. (2016) from which we calculate synthetic *TESS* observations. Marker colours, shapes, and shades have the same meaning as in Fig. 4.

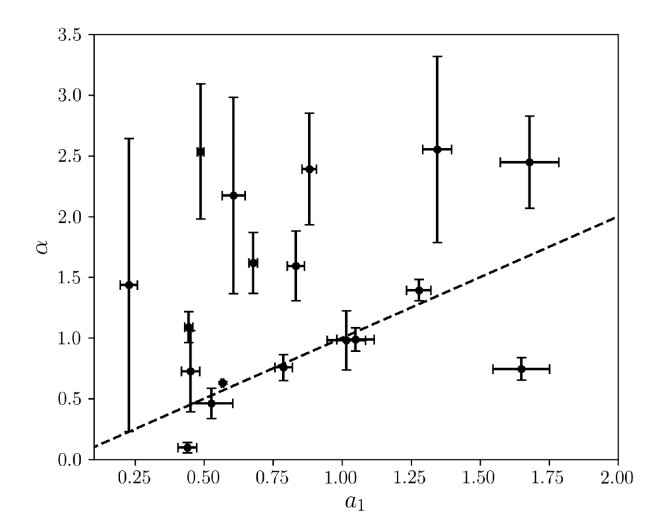


**Figure 6.** Comparing the initial rise indices from the single-component  $(\alpha)$  and curved power-law  $(a_1)$  forms. The dashed line indicates  $a_1 = \alpha$ . For well-constrained values of  $\alpha$ , the two fits agree quite well, but for poorly constrained values the single-component fits are consistently larger than those from the curved power-law fits.

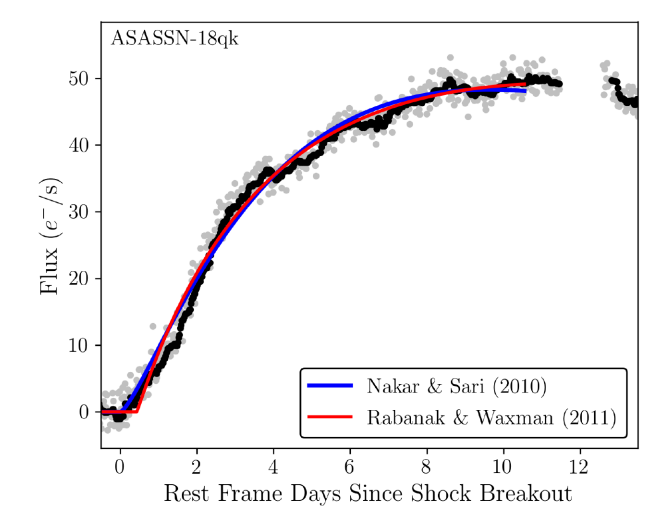
The semi-analytic models are very weakly dependent on progenitor mass.

The results are shown in Fig. 7. While these models fit the *TESS* data well, we find that they require implausibly large explosion energies and small progenitor radii. For example, ASASSN-18qk is best fit with an explosion energy of  $35 \times 10^{51}$  erg and a progenitor radius of  $22\,R_\odot$  in the Rabinak & Waxman (2011) treatment and

with an explosion energy of  $46 \times 10^{51}$  erg and a progenitor radius of  $29\,R_\odot$  in the Nakar & Sari (2010) treatment. These fits to ASASSN-18qk are shown in the top panel of Fig. 7, and the best-fitting values for the SNe II sample are shown in the lower panel. The explosion energies estimated from these fits are more than an order of magnitude larger than the typical  $\sim \! 10^{51}$  erg values expected for corecollapse events, pushing well into the extreme energy regimes of the pair-instability mechanism (Barkat, Rakavy & Sack 1967; Woosley, Blinnikov & Heger 2007; Kasen, Woosley & Heger 2011). The inferred  $\lesssim \! 100\,R_\odot$  radii are also implausibly small when compared to the observed  $500{-}1000\,R_\odot$  radii of RSGs (see e.g. Levesque et al. 2005).

Sapir & Waxman (2017) provide a likely explanation for these results. A fundamental assumption of these semi-analytic models is that the ejecta opacity remains constant over time, meaning that T will depend primarily on R. This assumption is reasonable for hydrogen dominated ejecta as long as  $T \gtrsim 8100 \,\mathrm{K} = T_R$ . At lower temperatures, recombination becomes important and modifies the opacity, complicating the relationship between T and R (See fig. 1 of Sapir & Waxman 2017). At longer wavelengths ( $\lambda_{\text{lim}} > hc/4k_BT_R \approx$ 4400 Å) like those of the TESS filter, the light-curve peak occurs after recombination becomes significant and the assumption of constant opacity no longer holds. Additionally, the longer rise times associated with redder filters exacerbate potential issues with shell curvature (equation 17 in Rabinak & Waxman 2011). In practice, this means that these models will become increasingly inaccurate for filters at wavelengths longer than that of the U-band (See Section 6.3 of Sapir & Waxman 2017).

While *Kepler* observations use a shorter wavelength filter than *TESS*, they are not particularly well-suited to this treatment either, as the *Kepler* bandpass covers 4200–9000 Å, peaking at 5750 Å (Van



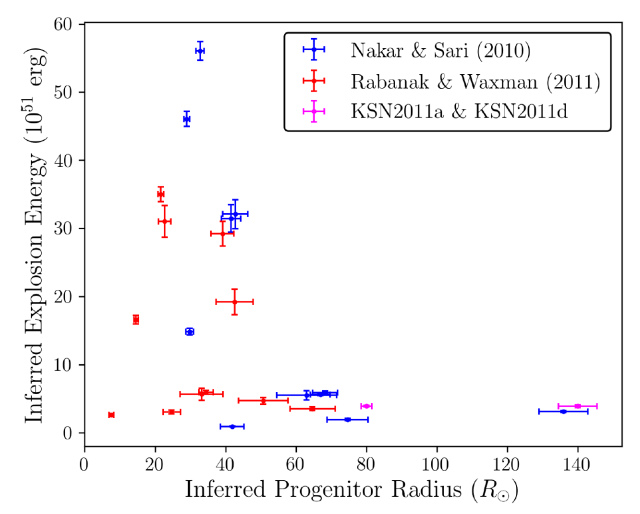


**Figure 7.** Fits to *TESS* data using the semi-analytic models of Nakar & Sari (2010) and Rabinak & Waxman (2011). The top panel shows the best-fitting models for ASASSN-18qk, a representative example of the fits obtained for the SNe II sample. After assuming a 12.5  $M_{\odot}$  progenitor, the best-fitting Nakar & Sari (2010) model implies a progenitor radius of  $29\,R_{\odot}$  and an explosion energy of  $46\times10^{51}$  erg, while the best-fitting Rabinak & Waxman (2011) model implies a progenitor radius of  $22\,R_{\odot}$  and an explosion energy of  $35\times10^{51}$  erg. Such implausible combinations of small radii and large explosion energies are a general feature of using these semi-analytic models to fit *TESS* observations. This can be seen in the lower panel, which shows the best-fitting parameters for the 11 well-observed SNe II in our sample. Updated fit parameters for KSN2011a and KSN2011d (shown in magenta) are also included in the lower panel.

Cleve & Caldwell 2016). In their Rabinak & Waxman (2011) models of the *Kepler* SNe KSN2011a and KSN2011d, Garnavich et al. (2016) note that the radii of 280 and 490 R $_{\odot}$  they obtain are also small when compared to those observed for RSGs. Their analysis differs from ours somewhat in that they assume  $f_p = 1.0$  and use  $T_{\rm ph}$  for their modelling. Note that there is a typo in their text stating that the models were computed using a density parameter of  $f_p = 0.1$ . If we make the same assumptions as Garnavich et al. (2016), we replicate their results. When we re-fit the KSN2011a and KSN2011d data instead using  $T_{\rm col}$  and assuming  $f_p = 0.1$ , we find that the explosion energy for both events increases from 2.0 to  $3.9 \times 10^{51}$  erg, and the progenitor radii are reduced by more than 70 per cent, to 80 and  $140 \, {\rm R}_{\odot}$ , respectively. Morozova et al. (2016) also noted that fitting the semi-

analytic Nakar & Sari (2010) model to their synthetic light curves led to overestimates of the explosion energy and underestimates of the progenitor radius. We will explore the question of whether these semi-analytic treatments can be empirically calibrated using the more detailed numerical models in Section 4.3

### 4.2 Numerical simulations

Next, we compare our observations to the suite of 126 numerical SNe IIP simulations presented by Morozova et al. (2016). Morozova et al. (2016) used the stellar evolution codes MESA (Paxton et al. 2011, 2013, 2015) and KEPLER (Weaver, Zimmerman & Woosley 1978; Woosley & Heger 2007, 2015; Sukhbold & Woosley 2014; Sukhbold et al. 2016) to produce two sets of non-rotating, solar-metallicity red supergiant (RSG) stars to serve as progenitors. To minimize confusion, we will refer to the stellar evolution code as KEPLER and the spacecraft as *Kepler*.

There are 23 KEPLER models in total, ranging in zero-age main-sequence (ZAMS) mass from 9 to  $20\,\mathrm{M}_\odot$ , and 19 MESA models ranging in ZAMS mass from 11 to  $20\,\mathrm{M}_\odot$ , both in increments of  $0.5\,\mathrm{M}_\odot$ . Morozova et al. (2016) explode these progenitor models using the SuperNova Explosion Code (SNEC; Morozova et al. 2015), which also generates both bolometric and filter-specific light curves. Using what is often referred to as the "thermal bomb" mechanism, SNEC initiates the explosions by injecting energy into the inner regions of the progenitor model after excising the innermost  $1.4\,\mathrm{M}_\odot$  to simulate the newly formed compact object. The amount of energy injected is chosen to yield the desired explosion energy. For each of the 42 progenitor models, this process is repeated three times to produce final (asymptotic) explosion energies of  $E_{\rm fin}=0.5, 1.0$ , and  $2.0\,\mathrm{foe}$ , where one foe is  $10^{51}\,\mathrm{erg}$ .

For the MESA models with ZAMS masses  $\gtrsim 15\,M_\odot$ , mass-loss is so significant that a larger ZAMS mass does not lead to larger pre-explosion mass. For example, both the 20 and 12.5  $M_\odot$  ZAMS mass MESA progenitors have pre-explosion masses of  $\sim 11\,M_\odot$ . This leads to the features seen in several of the Fig. 8 panels, and is ultimately a product of the strong de Jager, Nieuwenhuijzen & van der Hucht (1988) wind mass-loss prescription used for the MESA models. This prescription is argued to over-estimate the mass-loss rate (e.g. Smith 2014). The KEPLER models use the Nieuwenhuijzen & de Jager (1990) mass-loss prescription, where this effect is only seen for ZAMS masses above 23  $M_\odot$ , beyond the range of masses considered by Morozova et al. (2016). We will focus primarily on comparisons to the KEPLER models in our discussion.

The Morozova et al. (2016) analysis focuses on synthetic g-band observations, but since SNEC models SN emission as a blackbody, we can convert the bolometric luminosity and absolute g-band magnitudes from their work (all of which are available online at https://stellarcollapse.org/Morozova2016) into synthetic TESS observations. We use the PYSNPHOT package (STScI Development Team 2013) to compute absolute g-band magnitudes and bolometric luminosities for a large sequence of  $R_{\odot}$  blackbodies with 1 K spacing in  $T_{\rm eff}$  from 3000 to 303 000 K. To match the Morozova et al. (2016) models, we first use

$$\log[L] = \log[L(T_{\text{eff}}, R_{\odot})] + 2\log[R/R_{\odot}] \tag{4}$$

to determine the blackbody radius R necessary to match the bolometric luminosity for each  $R_{\odot}$  blackbody in our grid. We then use

$$M_g = M_g(T_{\text{eff}}, R_{\odot}) - 5\log[R/R_{\odot}]$$
 (5)

to determine which combination of  $T_{\text{eff}}$  and R best matches the SNEC data, and this process is repeated for each epoch in the synthetic

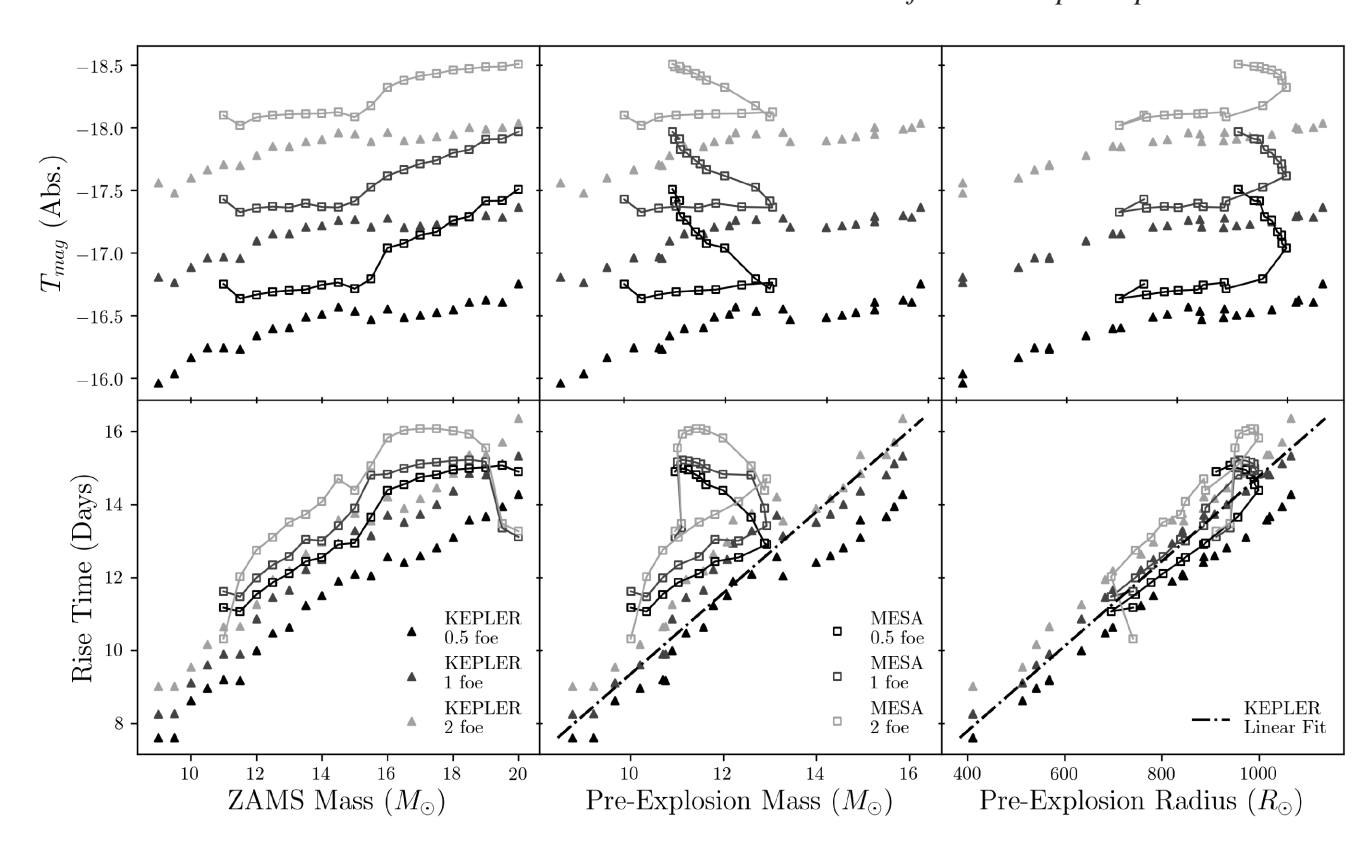


**Figure 8.** Peak absolute *TESS* magnitude and rise time for the synthetic light curves computed by Morozova et al. (2016) compared to the ZAMS mass, pre-explosion mass, and pre-explosion radius of the simulated progenitors. Progenitors simulated using MESA are shown as open squares, and those simulated using KEPLER are shown as solid triangles. Explosion energy is indicated by shading, with lighter shades corresponding to higher explosion energy. The MESA simulations are connected by solid lines to make the effects of their mass-loss prescription clear. Note that a "foe" is equal to 10<sup>51</sup> erg.

light curves. Three representative examples of these synthetic *TESS* observations are shown in Fig. 9, and *TESS*-band versions of all 126 model light curves from Morozova et al. (2016) are included in the online supplementary material.

We fit the curved power-laws to the synthetic data after excluding the shock breakout feature, as SNEC light curves are unreliable for the first  $\sim$ 1/4 d before the photosphere recedes and becomes better resolved (Morozova et al. 2015). These fits are shown by the red curves in Fig. 9, and as was found for the observed light curves, equation (2) fits the rising phases of the model light curves very well. The *TESS*-band peak absolute magnitude and rise time for all of the Morozova et al. (2016) models are shown in Fig. 8 as a function of their ZAMS mass, pre-explosion mass, and pre-explosion radius.

To first order, these synthetic *TESS* light curves are comparable to the observed sample. Like the observed sample, the model light curves have rise times of order two weeks and peak absolute *TESS*-band magnitudes of approximately -18 mag. In detail, however, the two samples differ somewhat. Notably, the Morozova et al. (2016) light curves cluster in relatively confined portions of parameter space compared to the significant diversity exhibited by the observed SNe. This is particularly evident in the  $\alpha$  and  $a_2$  distributions shown in Figs 4 and 5, respectively. There are also differences in the peak brightness, as even the brightest model light curves only attain absolute *TESS*-magnitudes of about -18.5 mag, a mark exceeded by several SNe II in our sample.

Examining the relationships shown in Fig. 8, a number of trends are readily apparent. First, larger explosion energies and larger progenitors tend to produce slower rising, more luminous light curves, with

the peak luminosity being driven primarily by the explosion energy and rise time being driven primarily by the progenitor size, just as in the semi-analytic models. For the KEPLER models there is a tight linear correlation between rise time and both ZAMS mass and pre-explosion mass. There are similar correlations for the lower ZAMS mass MESA models, but they are complicated at higher masses by the effects of mass loss. Morozova et al. (2016) found that there is a strong correlation between *g*-band rise time and progenitor radius. The rise times are naturally longer for the redder *TESS*-band, but the correlations between the rise time and the mass or radius are retained. While we focus our subsequent fits on the KEPLER models, the MESA models follow essentially the same radius-rise time relation.

The tight relation between progenitor radius and rise time for the KEPLER models shown in Fig. 8 is well-fit by

$$R/R_{\odot} = 85.8 \cdot (t_{\text{rise}}/d) - 267.6,$$
 (6)

with a scatter of  $\sigma_R = 58.9 \, R_\odot$  in radius. We obtain a similar fit for the KEPLER models between progenitor mass and rise time of

$$M/M_{\odot} = 0.897 \cdot (t_{\rm rise}/d) + 1.61,$$
 (7)

with a scatter of  $\sigma_M=0.77\,M_\odot$  in mass. This fit is slightly less robust than that obtained for the progenitor radii, and it will lead one to mildly overestimate masses for models of  $\sim\!12\text{--}14\,M_\odot$  progenitors and mildly underestimate masses for models of  $\sim\!14\text{--}16\,M_\odot$  progenitors.

Fig. 10 shows a histogram of the radius estimates for the twelve SNe II in our sample, using the above relations to convert their measured rise times to estimates of their progenitor radii and masses.

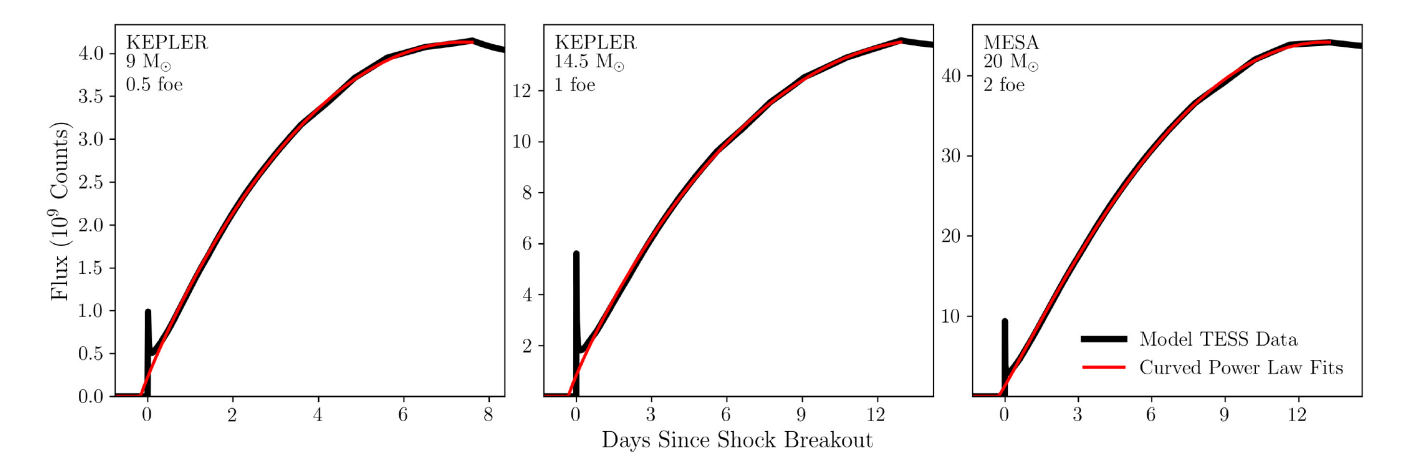


**Figure 9.** Examples of curved power-law fits to synthetic light curves calculated from the simulations of Morozova et al. (2016). The explosion energy and progenitor mass of the models increases from left- to right-hand panel. The left-hand and middle panels show KEPLER progenitors, while the right-hand panel shows a MESA progenitor. For each light curve, the synthetic *TESS* data is shown in black, and the best-fitting curve is shown in red. The brief shock breakout spike at the start of the light curves is excluded from the fits.

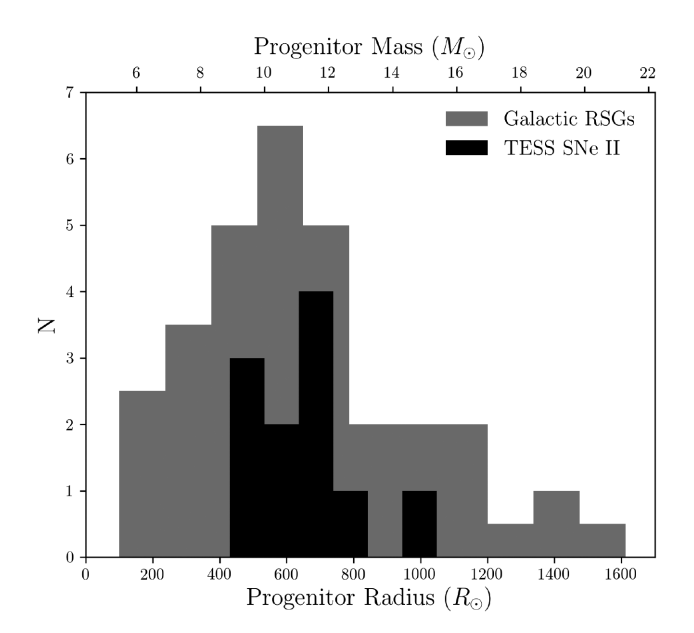


**Figure 10.** Comparison between the inferred radii of the SNe II progenitors in our sample and the stellar radius estimates of the Galactic RSGs studied by Levesque et al. (2005). To ease comparison, the Galactic RSG bins have been scaled down by a factor of two. The two distributions are broadly similar, and both have median values around  $R \sim 640 \, \mathrm{R}_{\odot}$ , corresponding to  $M \sim 11 \, \mathrm{M}_{\odot}$ .

For comparison, we also include a histogram of the 62 Galactic RSGs for which Levesque et al. (2005) were able to obtain radius estimates from MARCS stellar atmosphere models (Plez 2003; Gustafsson et al. 2003). The two distributions are broadly similar, each with median values near  $R\sim 640\,{\rm R}_\odot$  (corresponding to  $M\sim 11\,{\rm M}_\odot$ ). It is worth noting that this result stands in some contrast to the Sloan Digital Sky Survey and Supernova Legacy Survey SNe II sample of González-Gaitán et al. (2015), which favours progenitors smaller than  $400\,{\rm R}_\odot$ . Given that González-Gaitán et al. (2015) use the Nakar & Sari (2010) and Rabinak & Waxman (2011) models to estimate progenitor radii, it is likely that this discrepancy is another example of radius underestimation from the semi-analytic models.

# 4.3 Semi-analytic model calibration

While the physical values inferred from the Nakar & Sari (2010) and Rabinak & Waxman (2011) models are implausible, the fits themselves are quite good (e.g. the top panel of Fig. 7). Here, we investigate the possibility of calibrating the semi-analytic treatments using the models from Morozova et al. (2016). To do this, we fit the rising light curves of all 126 Morozova et al. (2016) models using the Nakar & Sari (2010) and Rabinak & Waxman (2011) treatments, adopting the same fixed  $12.5\,\mathrm{M}_\odot$  progenitor mass as in Section 4.1 to facilitate consistent comparisons. Repeating this procedure using the true SNEC progenitor mass instead of a fixed value has no significant effect on the results because the semi-analytic models are only weakly dependent on progenitor mass.

The left-hand and centre panels of Fig. 11 show the progenitor radii and explosion energies inferred by the semi-analytic treatments as a function of the true values in the Morozova et al. (2016) SNEC simulations. Consistent with our earlier results and the discussion in Morozova et al. (2016), the Nakar & Sari (2010) and Rabinak & Waxman (2011) fits underestimate the true radii and overestimate the true explosion energies by considerable margins. They are, however, reasonably well-correlated.

As a first experiment, we used linear fits to the correlations in Fig. 11 to re-calibrate the semi-analytic results. These best-fitting lines are shown as the dot-dashed lines in Fig. 11. For the Nakar & Sari (2010) treatment, the best-fitting calibration curves are

$$R_{\text{NS10}} = -9.2 + 0.138 \times R_{\text{SNEC}},$$
 (8)

and

$$E_{\text{NS10}} = -0.60 + 4.16 \times E_{\text{SNEC}}.$$
 (9)

In these expressions, radii are in units of  $R_{\odot}$  and explosion energies are given in units of  $10^{51}$  erg. The residual scatters about the fits are  $\sigma_R = 13.5 \, R_{\odot}$  and  $\sigma_E = 1.3 \times 10^{51}$  erg, respectively. For the Rabinak & Waxman (2011) treatment, the best-fitting calibration curves are

$$R_{\text{RW}11} = -51.0 + 0.186 \times R_{\text{SNEC}} \tag{10}$$

and

$$E_{\text{RW}11} = 0.37 + 1.81 \times E_{\text{SNEC}}.$$
 (11)

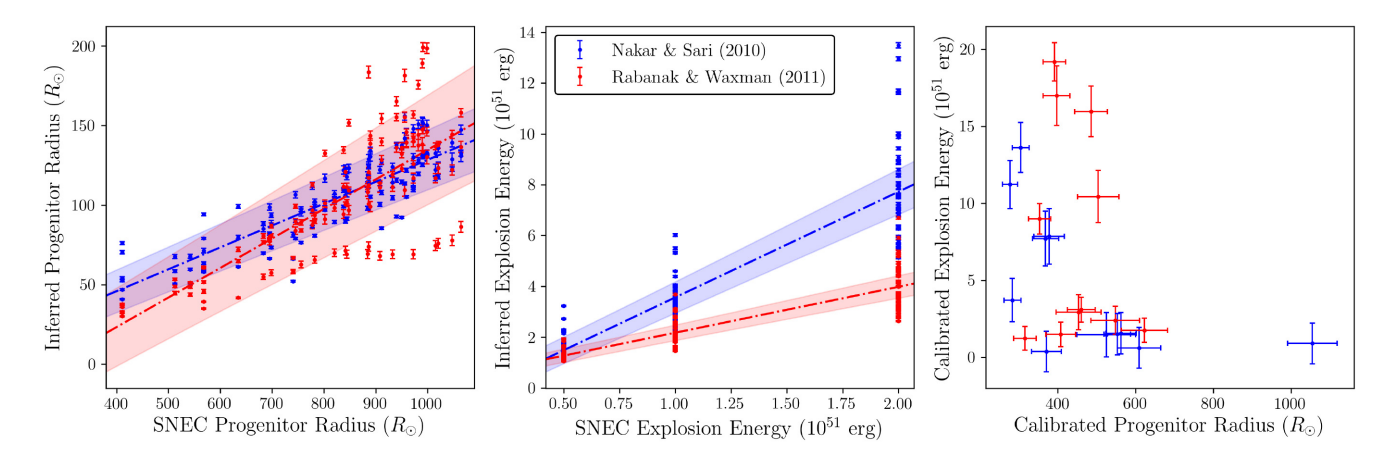


Figure 11. The semi-analytic models of Nakar & Sari (2010) and Rabinak & Waxman (2011) calibrated using the known progenitor properties of the Morozova et al. (2016) SNEC models. The left-hand and centre panels show the model parameters obtained when fitting the rising light curves of the Morozova et al. (2016) light curves using the Nakar & Sari (2010) and Rabinak & Waxman (2011) treatments. The semi-analytic fits shown here assume a progenitor mass of  $12.5\,\mathrm{M}_\odot$ . The left-hand panel shows the progenitor radii inferred by the semi-analytic models as a function of the actual SNEC progenitor radius, and the centre panel shows the inferred explosion energy as a function of its true value. Blue markers indicate the Nakar & Sari (2010) values, and red markers indicate the Rabinak & Waxman (2011) values. Best-fitting lines to each set of models are shown by the dot–dashed lines, and the shaded regions indicate the 95 per cent confidence interval for the fits. The right-hand panel shows the best-fitting parameters for the 11 well-observed SNe II in our sample after calibrating their semi-analytic fit parameters using the best-fitting relations for progenitor radius and explosion energy. This procedure leads to more physically reasonable values, although the inferred explosion energies are still quite high.

The scatters about these fits are  $\sigma_R=24.8\,\mathrm{R}_\odot$  and  $\sigma_E=0.6\times10^{51}\,\mathrm{erg}.$ 

We then use these fits to calibrate the inferred progenitor radii and explosion energy estimates obtained from the Nakar & Sari (2010) and Rabinak & Waxman (2011) models. Doing so, we obtain the right-hand panel of Fig. 11. Compared to the non-calibrated model parameters shown in the lower panel of Fig. 7, the calibrated parameters are considerably more reasonable, particularly the radius estimates. While improved from the non-calibrated explosion energy estimates (which are in many cases larger than 30 or even  $50 \times 10^{51}$  erg), the explosion energy estimates remain about an order of magnitude larger than expected values, even after calibration. Since the peak luminosity is driven primarily by the explosion energy, this discrepancy may be due to the limited range of luminosities attained by the Morozova et al. (2016) models. This forces significant extrapolation of the explosion energy calibration in order to match the high luminosity observed events.

As a second experiment, we also investigated adjusting the scaling factors used in the Nakar & Sari (2010) and Rabinak & Waxman (2011) models. Neglecting the brief initial planar phase, the Nakar & Sari (2010) model becomes

$$\frac{L_{\rm NS10}}{L_{\rm scale}} = \left(\frac{M}{15~{\rm M}_{\odot}}\right)^{-0.87} \left(\frac{R}{500~{\rm R}_{\odot}}\right) \left(\frac{E}{10^{51}~{\rm erg}}\right)^{0.96} \left(\frac{t}{\rm d}\right)^{-0.17}, \tag{12}$$

$$\frac{T_{\rm NS10}}{T_{\rm scale}} = \left(\frac{M}{15 \,\mathrm{M}_{\odot}}\right)^{-0.13} \left(\frac{R}{500 \,\mathrm{R}_{\odot}}\right)^{0.38} \left(\frac{E}{10^{51} \,\mathrm{erg}}\right)^{0.11} \left(\frac{t}{\mathrm{d}}\right)^{-0.56},\tag{13}$$

where we will solve for the scaling factors  $L_{\rm scale}$  and  $T_{\rm scale}$ . For the Rabinak & Waxman (2011) models, we again include a 1.23 scaling factor to convert  $T_{\rm ph}$  to  $T_{\rm col}$  and then solve for the scaling factors in their equations (13) and (14). Starting from the known progenitor masses, radii and explosion energies from the Morozova et al. (2016) SNEC models, we treat the factors in front of the blackbody prescriptions as free parameters.

Fig. 12 shows the scaling factor values that best fit the TESSband light curves of the Morozova et al. (2016) models, as well as their nominal values from Nakar & Sari (2010) and Rabinak & Waxman (2011). The values needed to fit the light curves given the true progenitor radii and explosion energies are quite different from the original models. The scaling factors from Nakar & Sari (2010) are  $L_{\rm scale}=3\times10^{42}~{\rm erg~s^{-1}}$  and  $T_{\rm scale}=3~{\rm eV}$ , while the fits indicate  $L_{\rm scale}=(1.2\pm0.2)\times10^{42}~{\rm erg~s^{-1}}$  and  $T_{\rm scale}=1.54\pm0.07~{\rm eV}$ . Similarly, the scaling factors from Rabinak & Waxman (2011) are  $r_{\rm scale} = 3.3 \times 10^{14} \, {\rm cm}$  and  $T_{\rm scale} = 1.6 \, {\rm eV}$ , while the fits indicate  $r_{\rm scale} = (4.5 \pm 0.3) \times 10^{14} \, {\rm cm} \text{ and } T_{\rm scale} = 0.95 \pm 0.06 \, {\rm eV}. \text{ Using}$ the updated scaling factors inferred by these fits, we obtain the progenitor radii and explosion energy estimates shown in the righthand panel of Fig. 12. These estimates follow the same trends of the prior calibration experiment. The calibrated radii estimates are reasonable, while the explosion energy estimates remain implausibly high for a significant portion of the events.

While these experiments are clearly not an immediate solution to the problem, they are a promising first step indicating that an empirical calibration is potentially feasible. Future work using numerical models that cover a wider range of parameter space and more complicated means of modifying the blackbody prescriptions of Nakar & Sari (2010) and Rabinak & Waxman (2011) is likely to prove worthwhile.

# 5 SHOCK BREAKOUT SIGNATURES

One notable feature of the Morozova et al. (2016) models discussed in Section 4.2 that we do not find in the observed sample is the unmistakable shock breakout spikes at the start of the SN light curves. The strength of this signal varies among the synthetic light curves, but it typically reaches  $\gtrsim 30$  per cent of the peak brightness (see Fig. 9). The time-steps used in the publicly available light curve files from Morozova et al. (2016) are just under 30 min, almost identical to the exposure length for a *TESS* FFI, so we might expect to see a signal of similar strength in the observations. However, visual inspection of the SNe light curves in Fig. 3 shows that this is not the case.

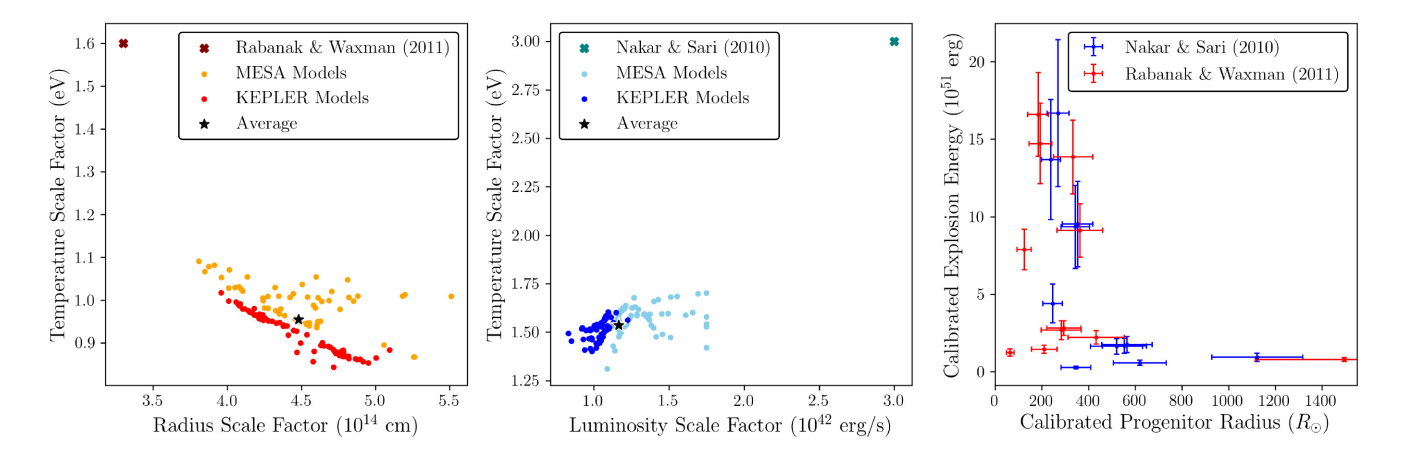


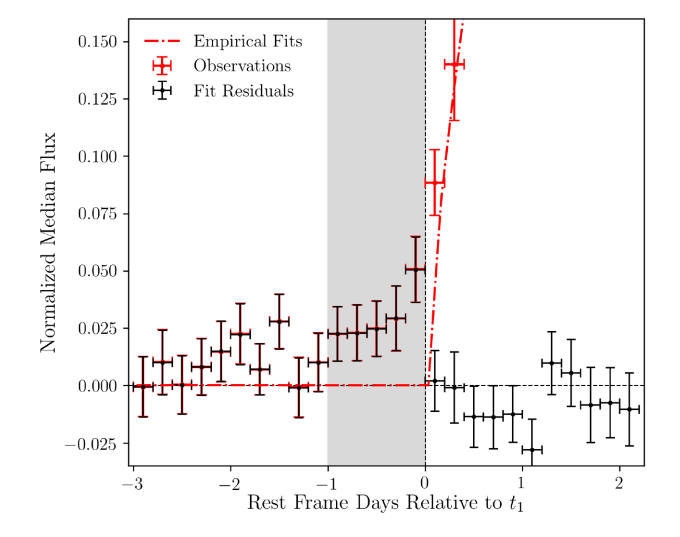
Figure 12. Calibrating the scaling factors of the semi-analytic Nakar & Sari (2010) and Rabinak & Waxman (2011) models using the Morozova et al. (2016) SNEC models. The maroon and teal crosses in the upper corners mark the original scaling factors for the Nakar & Sari (2010) and Rabinak & Waxman (2011) descriptions, respectively. Fits to the explosions of MESA progenitors are shown in orange and cyan, while those of KEPLER progenitors are shown in red and blue. The average scaling factors for both sets of models are shown by the two black stars. The right-hand panel shows the best-fitting parameters for the 11 well-observed SNe II in our sample when the semi-analytic models are updated to use these inferred scaling factors instead of their nominal values. As in Fig. 11, this calibration produces physically plausible radius estimates, but the inferred explosion energies remain implausibly high for many of the observed SNe II.

The existence of shock-breakout emission is a robust prediction of core-collapse theory that has been detected previously in observations at shorter wavelengths, so it is very likely present in the *TESS* data and is merely weaker than the SNEC models predict. That SNEC would simulate shock breakout imperfectly is not surprising. Morozova et al. (2015) note that during shock breakout the photosphere is in the outermost grid cell of the simulation and is spatially poorly resolved, rendering light curves in this early phase unreliable. They also note that the code assumes local thermodynamic equilibrium (LTE), imposing the same temperature for radiation and matter, an invalid approximation during shock breakout.

Shock breakout occurs on a time-scale comparable to the progenitor's light crossing time,  $t_{\rm lc} = R_*/c$ . For the  $\sim$ 640 R $_{\odot}$  progenitors in our sample, this corresponds to a duration of about 30 min. Because of this short time-scale, averaging over the FFIs may not aid in the detection of the shock breakout peak for an individual SN because it smears the peak out. We can, however, look for excess emission near the inferred time of first light,  $t_1$  averaged over multiple SNe.

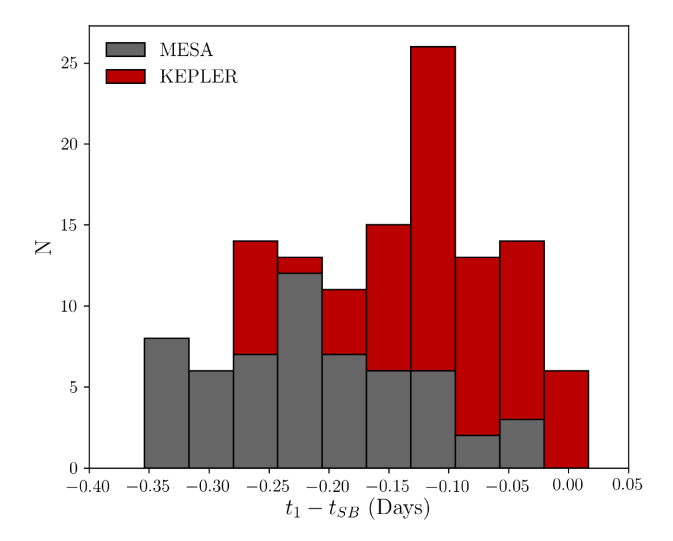
To do this, we stack the fit residuals for the 11 non-CSM interacting SNe II observed by TESS prior to explosion, subtract the best-fitting curved power laws from their observed light curves and combine all of the residuals. The CSM interacting SNe IIn are excluded from this analysis because the shock breakout signature is expected to be reprocessed and diluted by the dense CSM surrounding these SNe. Fig. 13 shows the resulting median residuals, focused on the timescales where we would expect to find shock-breakout emission and normalized such that the peak flux of the light curve is unity. There is a readily apparent excess visible in the residuals, peaking at  $3\sigma$ significance just prior to  $t_1$ , the time when the power-law rise begins. The cumulative significance of the excess feature reaches  $5\sigma$  when we incorporate all of the residuals in the 1 d prior to  $t_1$ , the shaded region shown in Fig. 13. It is possible that this excess is due to other factors, but it is plausibly associated with shock break out, so we will proceed under this assumption.

The emission clearly is not a sharp spike, but we would not expect to see one in these stacked residuals. The first issue is that the signals from the individual SNe will be in misaligned in time by any errors



**Figure 13.** Stacked light curves of the 11 non-CSM interacting SNe II in our sample near the time of first light. Residuals, shown in black, are calculated by subtracting the best-fitting curved power laws from the observed light curves, shown in red. Horizontal error bars represent the time interval for each bin, and vertical error bars show the  $1\sigma$  uncertainty in the median for the stacked fluxes and residuals from each bin. There is a clear, statistically significant excess visible in the stacked observations clustered just prior to  $t = t_1$ , the same time where we would expect to find signatures of shock breakout. We find a  $3\sigma$  excess at  $t - t_1 = -0.1$  d, and this grows to  $> 5\sigma$  significance when we include all of the bins from  $t_1 - 1.0$  to  $t_1$  d (the shaded region shown above).

in the estimate of the time of first light  $t_1$ . The measurement errors in  $t_1$  are typically 0.25 d (Tab. 2), but there are also probably systematic errors. To explore this question, we show the distribution of time differences between our fits to the Morozova et al. (2016) models for  $t_1$  and the actual time of shock breakout in the top panel of Fig. 14. This suggests that we might expect additional systematic shifts of 0.1–0.4 d. So in the stacked residuals, the signal will likely



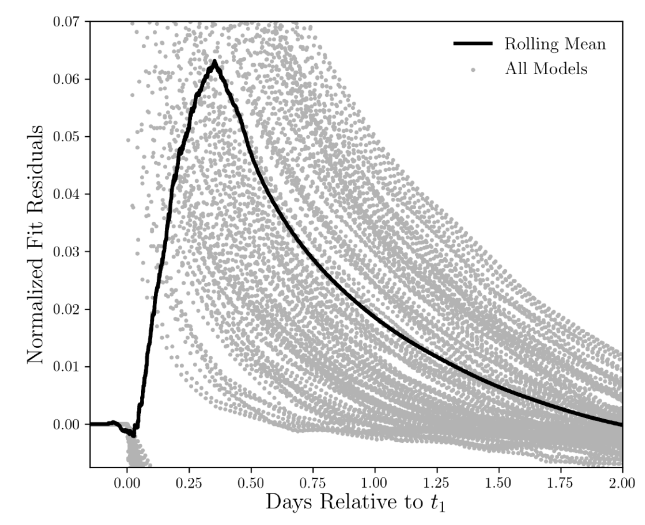


**Figure 14.** Histograms of the offsets between the inferred time of first light  $(t_1)$  and the time of shock breakout  $(t_{SB})$  for the fits to the 126 synthetic light *TESS* light curves calculated from the Morozova et al. (2016) models are shown in the top panel. The KEPLER models are shown in scarlet, and MESA models are shown in grey. Such offsets will contribute to temporally smearing the shock break out emission in Fig. 13. The bottom panel shows the curved power-law fit residuals for all of the Morozova et al. (2016) models in grey, and a 6-h rolling mean of all models in black. It is unlikely that the strength of the shock breakout excess seen here is meaningful given the limitations of the SNEC treatment at early times, but it illustrates how shock breakout can produce signatures spanning  $\sim$ 1 d in the stacked residuals.

be smeared over  $\sim\!\!0.5\,\mathrm{d}$  just by the uncertainties in how to temporally align the events.

The second issue is that while the shock break out peak lasts only approximately the light crossing time  $t_{\rm lc}$ , it is followed by a slower phase in which the ejecta expand and cool nearly adiabatically before the rise to peak begins. The time-scale for this phase of 0.5–1.0 d for RSGs is comparable to the transition time-scale between the planar and spherical phases of the Nakar & Sari (2010) model. While dimmer than the initial spike, this tail is not negligible and will temporally broaden the signal. Combining these two effects, the structure of the residuals does not seem surprising. Indeed, we find an excess of similar duration when we examine the residuals from our fits to the Morozova et al. (2016) models (lower panel of Fig. 14).

Note that this excess occurs at  $t > t_1$  because the empirical fits tend to underestimate  $t_1$  relative to  $t_{SB}$  (see Fig. 9).

We can use the amplitude of the excess to roughly estimate (or limit) the amplitude of shock break out signals in the TESS band. The energy of the excess is  $E_{\rm ex} \simeq \epsilon F_{\rm peak} \Delta t$ , where  $\epsilon \simeq 0.025$  is the amplitude of the excess relative to the peak flux  $F_{\rm peak}$  and  $\Delta t \simeq 24$  h is the duration of the observed excess in Fig. 13. This must be equal to the energy in the break out pulses,  $F_{\rm SBO}$  ×  $t_{\rm SBO}$ , where  $F_{\rm SBO}$  is the mean flux over time  $t_{\rm SBO}$ . Combining these, we must have that  $F_{\rm SBO}/F_{\rm peak} \simeq \epsilon \Delta t/t_{\rm SBO}$ . Clearly, we cannot have that most of the shock break out energy is emitted in the light crossing time, since for  $t_{\rm SBO} \simeq t_{lc} \simeq 0.5$  h,  $F_{\rm SBO}/F_{\rm peak} \simeq 1.2$  would produce signals easily visible in Fig. 3. However, when the emission is spread across the overall time-scale of the initial decline,  $t_{\rm SBO} \simeq 12$  h for a 1 foe explosion of a 500 R<sub> $\odot$ </sub>/10 M $_{\odot}$  progenitor (Nakar & Sari 2010), then  $F_{\rm SBO}/F_{\rm peak} \simeq 0.05$ . Such a smaller amplitude signal would be relatively easy to hide for the present sample.

#### 6 DISCUSSION AND CONCLUSIONS

In this work, we have presented the first *TESS* observations of corecollapse SNe. Due to its large survey area and continuous monitoring, *TESS* is particularly well-suited for obtaining high-cadence early-time observations of bright extragalactic transients such as these SNe. However, aspects of the *TESS* images like their large pixel size, the straps, and the many scattered light artifacts can make analyzing these observations difficult. In Section 2, we have described an image subtraction pipeline that addresses the most common issues present in *TESS* data. We have optimized this pipeline for the study of extragalactic transients, but these techniques would likely be beneficial for other *TESS* applications as well.

We do not identify any strong trends between the parameters of our empirical light curve fits and the peak luminosities of the SNe. The semi-analytic models of Nakar & Sari (2010) and Rabinak & Waxman (2011) fit the data well, but the resulting estimates of the explosion energies and progenitor radii are not physical, probably because the TESS bandpass is too red. This also appears to be true for Kepler observations. Numerical light curves computed using SNEC yield more plausible estimates, and may provide a means through which the semi-analytic models can be calibrated. We briefly explored this possibility in Section 4.3 using two calibration methods. In the first, we used linear fits to calibrate the output energies and radii from the semi-analytic models such that they agree with those of the SNEC models. In the second, we use the known parameters from the SNEC models to update the scaling factors of the semianalytic models. The results of these two methods were comparable, producing more physically reasonable radius estimates and improved explosion energies, although even after calibration, the inferred explosion energies remained quite high. More complex approaches, like altering the exponents of the semi-analytic models, might yield better results.

Broadly speaking, the synthetic *TESS* light curves produced from the Morozova et al. (2016) models are comparable to what we observe in our sample. The empirical fit parameters for the two data sets are reasonably similar, the rise times are of order two weeks, and the peak absolute *TESS*-band magnitudes are of order –18 mag. In detail, however, the Morozova et al. (2016) models appear to differ somewhat from the observed light curves. The SNEC models cluster in relatively confined portions of parameter space compared to the observed light curves, failing to reproduce the full diversity implied by the observations. The observed power-law indices found for the rise tend to be shallower but also more diverse. Additionally,

even the most energetic SNEC explosions of the most massive model progenitors only reach absolute *TESS*-magnitudes of about -18.5 mag. Four of the twelve SNe II in our sample have higher peak luminosities.

A detailed study of these discrepancies is beyond the scope of this work, but we can consider potential explanations. When compared to other numerical models of core-collapse explosions, the Morozova et al. (2016) models are relatively simple. They do not include contributions from radioactive <sup>56</sup>Ni or interactions with CSM, for example. These simplifications allow Morozova et al. (2016) to study a range of models broadly dispersed throughout the progenitor size and explosion energy parameter spaces. In the absence of significant mixing, contributions from radioactive <sup>56</sup>Ni are likely small during the early rise of core-collapse light curves, but subsequent studies by Morozova, Piro & Valenti (2017, 2018) have argued that emission enhancement due to CSM interaction is an extremely important aspect of early SNe II light curves. Förster et al. (2018) make a similar argument when invoking the presence of dense winds or extended atmospheres to explain rapidly rising SN II light curves. It is, however, difficult to reconcile these scenarios with the quiescent pre-SN observations of Type II progenitors (Johnson, Kochanek & Adams 2018). Moreover, the dense winds invoked in these scenarios would blanket the stars in dust (see e.g. Kochanek 2011), rendering them optically invisible, and yet direct detections of progenitors are relatively common (Smartt et al. 2009; Smartt 2015).

A more likely explanation is that SN progenitors do not have the "sharp" edges in density assumed by stellar evolution models, instead having extensions to their envelopes driven by pulsations, which do not in turn produce high mass density winds. Additional problems may arise from simplifications in the SNEC treatment, like its assumption of LTE throughout the model. Morozova et al. (2018) note that while SNEC's bolometric light curves generally agree quite well with the multigroup radiation-hydrodynamic code STELLA (Blinnikov & Bartunov 1993, 2011), their synthetic filter light curves do exhibit minor discrepancies. More self-consistent explosion models, like those of the PUSH framework (Perego et al. 2015; Curtis et al. 2020), might also modify the very early light curves.

We find a mean pre-rise flux excess for the Type II SNe of  $\sim 2.5$  per cent of the peak flux in the  $\sim 1$  d before the estimated start of the rising light curve which is plausibly due to the shock break out. In this scenario, the excess cannot be dominated by energy from an initial peak lasting only the light crossing time ( $\sim$ 0.5 h), as this would lead to visible peaks in the individual light curve. The energy would have to be emitted over a longer time period. We roughly estimate that the signal should be directly detectable for an SNe II with a peak TESS magnitude brighter than about 15 mag. The switch from a 30-min cadence to a 10-min cadence in the extended TESS mission will make searches for such emission from stripped SNe more feasible. In addition to the bright SN Ibn and SN IIb presented here, TESS has already observed multiple SNe Ia (Fausnaugh et al. 2019) and a tidal disruption event (Holoien et al. 2019b) brighter than 15 mag, so it is very likely that TESS will observe a sufficiently bright SN II to allow a direct detection. Even without a direct detection, stacking analyses like that used here will steadily improve.

TESS provides a valuable new means of studying core-collapse SNe, one that will only become more significant as the sample of early-time TESS observations grows. Better models to interpret the early-time emission are clearly needed. In particular, (semi-analytic) models of both the shock break out peak, its decay and the initial rise appropriate for these redder bands would be very useful, as

would methods of using expensive numerical simulations to calibrate simpler models that can be easily fit to the data. With larger numbers of SNe, we would also hope to see clear statistical patterns begin to appear in the distributions and correlations of the parameters describing the initial light curve rises. As a continuing mission, there remains the chance of a spectacularly bright SN that can be followed in detail at the full TESS FFI cadence.

#### **ACKNOWLEDGEMENTS**

We thank the referee, Héloïse F. Stevance, for helpful comments. We greatly appreciate Viktoriya Morozova sharing model light curves with us, as well as Peter Garnavich's willingness to discuss semi-analytic modelling approaches and share some of the fitting code used in Garnavich et al. (2016). We would also like to thank Tuguldur Sukhbold, Eli Waxman, and Sanjana Curtis for valuable discussions. PJV is supported by the National Science Foundation Graduate Research Fellowship Program Under Grant No. DGE-1343012. CSK, KZS, and BJS are supported by NSF grant AST-1907570. CSK and KZS are also supported by NSF grant AST-181440. BJS is also supported by NASA grant 80NSSC19K1717 and NSF grants AST-1920392 and AST-1911074.

This paper includes data collected by the *TESS* mission, which are publicly available from the Mikulski Archive for Space Telescopes (MAST). Funding for the *TESS* mission is provided by NASA's Science Mission directorate. We thank Ethan Kruse for continuing to upload animations of the TESS FFIs to YouTube, as these videos have been invaluable for investigating the systematics in our data. In addition to the software cited in the main body of the paper, we have also made use of NUMPY (Harris et al. 2020), SCIPY (Virtanen et al. 2020), ASTROPY (Astropy Collaboration et al. 2013), PYRAF (Science Software Branch at STScI 2012), IPYTHON (Perez & Granger 2007), MATPLOTLIB (Hunter 2007), PANDAS (Wes McKinney 2010), and SAOIMAGE DS9 (Joye & Mandel 2003)

This work is heavily reliant on the ongoing All-Sky Automated Survey for Supernovae. We thank the Las Cumbres Observatory and its staff for its continuing support of the ASAS-SN project. ASAS-SN is supported by the Gordon and Betty Moore Foundation through grant GBMF5490 to the Ohio State University, and NSF grants AST-1515927 and AST-1908570. Development of ASAS-SN has been supported by NSF grant AST-0908816, the Mt. Cuba Astronomical Foundation, the Center for Cosmology and AstroParticle Physics at the Ohio State University, the Chinese Academy of Sciences South America Center for Astronomy (CAS-SACA), and the Villum Foundation.

In this work, we have made extensive use the ZTF alert broker Lasair (Smith et al. 2019) and the ZTF data it provides access to. Lasair is supported by the UKRI Science and Technology Facilities Council and is a collaboration between the University of Edinburgh (grant ST/N002512/1) and Queen's University Belfast (grant ST/N002520/1) within the LSST:UK Science Consortium. ZTF is supported by National Science Foundation grant AST-1440341 and a collaboration including Caltech, IPAC, the Weizmann Institute for Science, the Oskar Klein Center at Stockholm University, the University of Maryland, the University of Washington, Deutsches Elektronen-Synchrotron and Humboldt University, Los Alamos National Laboratories, the TANGO Consortium of Taiwan, the University of Wisconsin at Milwaukee, and Lawrence Berkeley National Laboratories. Operations are conducted by COO, IPAC, and UW. This research has made use of "Aladin sky atlas" developed at CDS, Strasbourg Observatory, France 2000A&AS..143...33B and 2014ASPC..485..277B.

## DATA AVAILABILITY

Both the observed *TESS* light curves we present here and the synthetic observations produced from the Morozova et al. (2016) simulations are available in machine-readable format in the online supplementary material.

### REFERENCES

Alard C., 2000, A&AS, 144, 363

Alard C., Lupton R. H., 1998, ApJ, 503, 325

Astropy Collaboration et al., 2013, A&A, 558, A33

Aydi E. et al., 2019, Astron. Telegram, 12889, 1

Baklanov P. V., Blinnikov S. I., Pavlyuk N. N., 2005, Astron. Lett., 31, 429

Barkat Z., Rakavy G., Sack N., 1967, Phys. Rev. Lett., 18, 379

Bellm E. C. et al., 2019, PASP, 131, 018002

Bersten M. C. et al., 2012, ApJ, 757, 31

Blinnikov S. I., Bartunov O. S., 1993, A&A, 273, 106

Blinnikov S. I., Bartunov O. S., 2011, STELLA: Multi-group Radiation Hydrodynamics Code, Astrophysics Source Code Library, Houghton, MI

Bose S., Holmbo S., Mattila S., Kankare E., Stritzinger M., Heikkila T., Chen P., 2019, Transient Name Serv. Classif. Rep., 1332, 1

Branch D., Wheeler J. C., 2017, Supernova Explosions, Springer-Verlag, Berlin

Brimacombe J. et al., 2018, Astron. Telegram, 11933, 1

Brimacombe J. et al., 2019, Astron. Telegram, 12657, 1

Brimacombe J. et al., 2020, Astron. Telegram, 13666, 1

Brinnel V., Carracedo A. S., Barbarino C., Tartaglia L., Yaron O., 2019, Transient Name Serv. Classif. Rep., 417, 1

Burke J., Hiramatsu D., Howell D. A., McCully C., Gonzalez E. P., Pellegrino C., 2020, Transient Name Serv. Classif. Rep., 1666, 1

Cacella P. et al., 2019, Astron. Telegram, 13326, 1

Calzavara A. J., Matzner C. D., 2004, MNRAS, 351, 694

Castro N. et al., 2019, Astron. Telegram, 12864, 1

Castro-Segura N., Pursiainen M., Smith M., Yaron O., 2018, Transient Name Serv. Classif. Rep., 2064, 1

Chasovnikov A. et al., 2018, Transient Name Serv. Discovery Rep., 1888, 1 Chugai N. N., Danziger I. J., 1994, MNRAS, 268, 173

Curtis S., Wolfe N., Fröhlich C., Miller J. M., Wollaeger R., Ebinger K., 2020, preprint (arXiv:2008.05498)

Dahiwale A., Fremling C., 2020, Transient Name Serv. Classif. Rep., 332, 1 de Jager C., Nieuwenhuijzen H., van der Hucht K. A., 1988, A&AS, 72, 259

Dessart L., Hillier D. J., Waldman R., Livne E., 2013, MNRAS, 433, 1745

Dessart L., Yoon S.-C., Livne E., Waldman R., 2018, A&A, 612, A61

Dimitriadis G. et al., 2019, ApJ, 870, L1

Ensman L., Burrows A., 1992, ApJ, 393, 742

Fausnaugh M. M. et al., 2019, preprint (arXiv:1904.02171)

Feinstein A. D. et al., 2019, PASP, 131, 094502

Filippenko A. V., 1997, ARA&A, 35, 309

Filippenko A. V., Matheson T., Ho L. C., 1993, ApJ, 415, L103

Forster F., 2019, Transient Name Serv. Discovery Rep., 1684, 1

Förster F. et al., 2018, Nature Astronomy, 2, 808

Forster F. et al., 2020a, Transient Name Serv. Discovery Rep., 1550, 1

Forster F. et al., 2020b, Transient Name Serv. Discovery Rep., 914, 1

Fremling C., 2018, Transient Name Serv. Discovery Rep., 1467, 1

Fremling C., Dugas A., Sharma Y., 2018, Transient Name Serv. Classif. Rep., 1870, 1

Fremling C., Dugas A., Sharma Y., 2019, Transient Name Serv. Classif. Rep., 670, 1

Frohmaier C. et al., 2019, Transient Name Serv. AstroNote, 31, 1

Gaia Collaboration et al., 2016, A&A, 595, A1

Galama T. J. et al., 1998, Nature, 395, 670

Garnavich P. M., Tucker B. E., Rest A., Shaya E. J., Olling R. P., Kasen D., Villar A., 2016, ApJ, 820, 23

Gezari S. et al., 2015, ApJ, 804, 28

González-Gaitán S. et al., 2015, MNRAS, 451, 2212

Gromadzki M., Dong S., Buckley D., 2019, Transient Name Serv. Classif. Rep., 812, 1

Gustafsson B., Edvardsson B., Eriksson K., Mizuno-Wiedner M., Jørgensen U. G., Plez B., 2003, in Hubeny I., Mihalas D., Werner K., eds, ASP Conf. Ser. Vol. 288, Stellar Atmosphere Modeling. Astron. Soc. Pac., San Francisco, p. 331

Haas M. R. et al., 2010, ApJ, 713, L115

Handberg R., Lund M. N., 2019, T'DA Data Release Notes – Data Release 4 for TESS Sectors 1 + 2, Zenodo, Meyrin, Switzerland

Harris C. R. et al., 2020, preprint (arXiv:2006.10256)

Hiramatsu D., Arcavi I., Burke J., Howell D. A., McCully C., Pellegrino C., Valenti S., 2019a, Transient Name Serv. Classif. Rep., 1557, 1

Hiramatsu D., Burke J., Arcavi I., Howell D. A., McCully C., Valenti S., 2019b, Transient Name Serv. Classif. Rep., 738, 1

Hodapp K. W. et al., 2019, AJ, 158, 241

Hodgkin S. T. et al., 2019, Transient Name Serv. Discovery Rep., 1300, 1

Holmbo S. et al., 2019, Astron. Telegram, 12661, 1

Holoien T. W. S. et al., 2019a, MNRAS, 484, 1899

Holoien T. W. S. et al., 2019b, ApJ, 883, 111

Hunter J. D., 2007, Comput. Sci. Eng., 9, 90

Irani I., Zimmerman E., Bruch R., Yaron O., 2020, Transient Name Serv. Classif. Rep., 369, 1

Jayasinghe T. et al., 2019, MNRAS, 493, 4186

Jenkins J. M. et al., 2016, Proc. SPIE Conf. Ser. Vol. 9913, Software and Cyberinfrastructure for Astronomy IV. SPIE, Bellingham, p. 99133E

Johnson S. A., Kochanek C. S., Adams S. M., 2018, MNRAS, 480, 1696

Joye W. A., Mandel E., 2003, in Payne H. E., Jedrzejewski R. I., Hook R. N., eds, ASP Conf. Ser. Vol. 295, Astronomical Data Analysis Software and Systems XII. Astron. Soc. Pac., San Francisco, p. 489

Kasen D., Woosley S. E., 2009, ApJ, 703, 2205

Kasen D., Woosley S. E., Heger A., 2011, ApJ, 734, 102

Klein R. I., Chevalier R. A., 1978, ApJ, 223, L109

Kochanek C. S., 2011, ApJ, 743, 73

Kochanek C. S. et al., 2017, PASP, 129, 104502

Leadbeater R., 2019, Transient Name Serv. Classif. Rep., 2506, 1

Levesque E. M., Massey P., Olsen K. A. G., Plez B., Josselin E., Maeder A., Meynet G., 2005, ApJ, 628, 973

Li W. et al., 2011, MNRAS, 412, 1441

Lipunov V. et al., 2010, Adv. Astron., 2010, 349171

Lipunov V. et al., 2019, Transient Name Serv. Discovery Rep., 760, 1

Lund M. N., Handberg R., Kjeldsen H., Chaplin W. J., Christensen-Dalsgaard J., 2017, European Physical Journal Web of Conferences, EDP Sciences, Les Ulis, France, p. 01005

Maund J. R., Smartt S. J., Kudritzki R. P., Podsiadlowski P., Gilmore G. F., 2004, Nature, 427, 129

Modjaz M. et al., 2009, ApJ, 702, 226

Morozova V., Piro A. L., Renzo M., Ott C. D., Clausen D., Couch S. M., Ellis J., Roberts L. F., 2015, ApJ, 814, 63

Morozova V., Piro A. L., Renzo M., Ott C. D., 2016, ApJ, 829, 109

Morozova V., Piro A. L., Valenti S., 2017, ApJ, 838, 28

Morozova V., Piro A. L., Valenti S., 2018, ApJ, 858, 15

Nakar E., Sari R., 2010, ApJ, 725, 904

Nicholls B. et al., 2018, Astron. Telegram, 11910, 1

Nieuwenhuijzen H., de Jager C., 1990, A&A, 231, 134

Nomoto K., Suzuki T., Shigeyama T., Kumagai S., Yamaoka H., Saio H., 1993, Nature, 364, 507

Nordin J., Brinnel V., Giomi M., Santen J. V., Gal-Yam A., Yaron O., Schulze S., 2019, Transient Name Serv. Discovery Rep., 1546, 1

Nordin J., Brinnel V., Giomi M., Santen J. V., Gal-Yam A., Yaron O., Schulze S., 2020a, Transient Name Serv. Discovery Rep., 177, 1

Nordin J., Brinnel V., Giomi M., Santen J. V., Gal-Yam A., Yaron O., Schulze S., 2020b, Transient Name Serv. Discovery Rep., 239, 1

Olling R. P. et al., 2015, Nature, 521, 332

Onori F., Stein R., Cannizzaro G., Yaron O., 2018a, Transient Name Serv. Classif. Rep., 1099, 1

Onori F., Stein R., Cannizzaro G., Yaron O., 2018b, Transient Name Serv. Classif. Rep., 1114, 1

Pál A. et al., 2020, ApJS, 247, 9

Paxton B., Bildsten L., Dotter A., Herwig F., Lesaffre P., Timmes F., 2011, ApJS, 192, 3

Paxton B. et al., 2013, ApJS, 208, 4

Paxton B. et al., 2015, ApJS, 220, 15

Payne A. V. et al., 2020, preprint (arXiv:2009.03321)

Perego A., Hempel M., Fröhlich C., Ebinger K., Eichler M., Casanova J., Liebendörfer M., Thielemann F. K., 2015, ApJ, 806, 275

Perez F., Granger B. E., 2007, Comput. Sci. Eng., 9, 21

Plez B., 2003, in Munari U., ed., ASP Conf. Ser. Vol. 298, GAIA Spectroscopy: Science and Technology. Astron. Soc. Pac., San Francisco, p. 189

Rabinak I., Waxman E., 2011, ApJ, 728, 63

Razza A., Pineda J., Gromadzki M., Yaron O., 2018, Transient Name Serv. Classif. Rep., 2015, 1

Ricker G. R. et al., 2015, J. Astron. Telesc. Instrum. Syst., 1, 014003

Sand D. J., Valenti S., Lundquist M., Amaro R., Wyatt S., 2018, Transient Name Serv. Discovery Rep., 2000, 1

Sand D., Valenti S., Amaro R., Lundquist M., Wyatt S., Andrews J., Dong Y., 2019, Transient Name Serv. Discovery Rep., 717, 1

Sapir N., Waxman E., 2017, ApJ, 838, 130

Schawinski K. et al., 2008, Science, 321, 223

Schlafly E. F., Finkbeiner D. P., 2011, ApJ, 737, 103

Schlegel E. M., 1990, MNRAS, 244, 269

Schlegel D. J., Finkbeiner D. P., Davis M., 1998, ApJ, 500, 525

Science Software Branch at STScI, 2012, PyRAF: Python alternative for IRAF, record ascl:1207.011

Shappee B. J. et al., 2014, ApJ, 788, 48

Shappee B. J. et al., 2016, ApJ, 826, 144

Shappee B. J. et al., 2019, ApJ, 870, 13

Smartt S. J., 2009, ARA&A, 47, 63

Smartt S. J., 2015, PASA, 32, e016

Smartt S. J., Eldridge J. J., Crockett R. M., Maund J. R., 2009, MNRAS, 395, 1409

Smith N., 2014, ARA&A, 52, 487

Smith K. W. et al., 2019, Res. Notes Am. Astron. Soc., 3, 26

Soderberg A. M. et al., 2008, Nature, 453, 469

Stanek K. Z. et al., 2003, ApJ, 591, L17

Stassun K. G. et al., 2018, AJ, 156, 102

Stevance H. F. et al., 2020, MNRAS, 494, 885

Stritzinger M. D. et al., 2018, ApJ, 864, L35

STScI Development Team, 2013, pysynphot: Synthetic photometry software package, record ascl:1303.023

Sukhbold T., Woosley S. E., 2014, ApJ, 783, 10

Sukhbold T., Ertl T., Woosley S. E., Brown J. M., Janka H. T., 2016, ApJ, 821, 38 Tartaglia L. et al., 2018, ApJ, 853, 62

Terreran G., 2019, Transient Name Serv. Classif. Rep., 1749, 1

Theureau G., Hanski M. O., Coudreau N., Hallet N., Martin J. M., 2007, A&A, 465, 71

Tomasella L., Benetti S., Cappellaro E., Elias-Rosa N., Turatto M., 2020, Transient Name Serv. Classif. Rep., 946, 1

Tonry J. L. et al., 2018, PASP, 130, 064505

Tonry J. et al., 2019a, Transient Name Serv. Discovery Rep., 399, 1

Tonry J. et al., 2019b, Transient Name Serv. Discovery Rep., 545, 1

Tucker M. A. et al., 2020, preprint (arXiv:2009.07856)

Utrobin V., 1993, A&A, 270, 249

Utrobin V. P., Wongwathanarat A., Janka H. T., Müller E., Ertl T., Woosley S. E., 2019, A&A, 624, A116

Vallely P. J. et al., 2019, MNRAS, 487, 2372

Van Cleve J. E., Caldwell D. A., 2016, Kepler Instrument Handbook, Mikulski Archive for Space Telescopes, Baltimore

van Roestel J. et al., 2019, Res. Notes Am. Astron. Soc., 3, 136

Virtanen P. et al., 2020, Nature Methods, 17, 261

Weaver T. A., Zimmerman G. B., Woosley S. E., 1978, ApJ, 225, 1021

Wes M., 2010, in van der Walt S., Millman J., eds, Proceedings of the 9th Python in Science Conference. SciPy, Austin, Texas, p. 56

Woosley S. E., 1988, ApJ, 330, 218

Woosley S. E., Heger A., 2007, Phys. Rep., 442, 269

Woosley S. E., Heger A., 2015, ApJ, 810, 34

Woosley S. E., Eastman R. G., Weaver T. A., Pinto P. A., 1994, ApJ, 429, 300

Woosley S. E., Blinnikov S., Heger A., 2007, Nature, 450, 390

Yao Y. et al., 2019, ApJ, 886, 152

Young T. R., 2004, ApJ, 617, 1233

Zhang J., Gal-Yam A., Wang L., Wang X., Xing L., Yang Y., Schulze A. S., 2020, Transient Name Serv. Classif. Rep., 1516, 1

## SUPPORTING INFORMATION

Supplementary data are available at MNRAS online.

# MorozovaSNECLightCurves.zip TESSLightCurves.zip

Please note: Oxford University Press is not responsible for the content or functionality of any supporting materials supplied by the authors. Any queries (other than missing material) should be directed to the corresponding author for the article.

This paper has been typeset from a TEX/LATEX file prepared by the author.